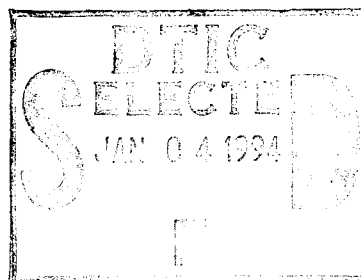


RL-TR-94-195
Final Technical Report
November 1994



HIGH-SPEED COHERENT LASER ARRAYS

David Sarnoff Research Center, Inc.



Sponsored by
Advanced Research Projects Agency
ARPA Order No. 8799

DTIC QUALITY INSPECTED 2

APPROVED FOR PUBLIC RELEASE; DISTRIBUTION UNLIMITED.

19941229 038

The views and conclusions contained in this document are those of the authors and should not be interpreted as necessarily representing the official policies, either expressed or implied, of the Advanced Research Projects Agency or the U.S. Government.

Rome Laboratory
Air Force Materiel Command
Griffiss Air Force Base, New York

This report has been reviewed by the Rome Laboratory Public Affairs Office (PA) and is releasable to the National Technical Information Service (NTIS). At NTIS it will be releasable to the general public, including foreign nations.

RL-TR-94-195 has been reviewed and is approved for publication.

APPROVED: *Ernst K Walge*

ERNST K. WALGE
Project Engineer

FOR THE COMMANDER: *Donald W Hanson*

DONALD W. HANSON
Director of Surveillance & Photonics

If your address has changed or if you wish to be removed from the Rome Laboratory mailing list, or if the addressee is no longer employed by your organization, please notify RL (OCPC) Griffiss AFB NY 13441. This will assist us in maintaining a current mailing list.

Do not return copies of this report unless contractual obligations or notices on a specific document require that it be returned.

HIGH-SPEED COHERENT LASER ARRAYS

Marc K. Felisky and Richard DeFreez (OGI)
Joseph H. Abeles, Daniel W. Bechtle, and S. Yegna Narayan

Contractor: David Sarnoff Research Center, Inc.
Contract Number: F30602-92-C-0111
Effective Date of Contract: 01 July 1992
Contract Expiration Date: 30 June 1993
Short Title of Work: High-Speed Coherent Laser Arrays
Period of Work Covered: Jul 92 - Jul 93

Principal Investigator: S. Yegna Narayan
Phone: (609) 734-2036
RL Project Engineer: Ernst K. Walge
Phone: (315) 330-3147

Approved for public release; distribution unlimited.

This research was supported by the Advanced Research Projects Agency of the Department of Defense and was monitored by Ernst K. Walge, RL (OCPC), 25 Electronic Pky, Griffiss AFB NY 13441-4515.

REPORT DOCUMENTATION PAGE

Form Approved
OMB No. 0704-0188

Public reporting burden for this collection of information is estimated to average 1 hour per response, including the time for reviewing instructions, searching existing data sources, gathering and maintaining the data needed, and completing and reviewing the collection of information. Send comments regarding this burden estimate or any other aspect of this collection of information, including suggestions for reducing this burden, to Washington Headquarters Services, Directorate for Information Operations and Reports, 1215 Jefferson Davis Highway, Suite 1204, Arlington, VA 22202-4302, and to the Office of Management and Budget, Paperwork Reduction Project (0704-0188), Washington, DC 20503.

1. AGENCY USE ONLY (Leave Blank)		2. REPORT DATE October 1994		3. REPORT TYPE AND DATES COVERED Final Jul 92 - Jul 93	
4. TITLE AND SUBTITLE HIGH-SPEED COHERENT LASER ARRAYS				5. FUNDING NUMBERS C - F30602-92-C-0111 PE - 61101E PR - H799 TA - 00 WU - 01	
6. AUTHOR(S) Marc K. Felisky and Richard DeFreez (OGI*) Joseph H. Abeles, Daniel W. Bechtle, and S. Yegna Narayan				7. PERFORMING ORGANIZATION NAME(S) AND ADDRESS(ES) David Sarnoff Research Center, Inc. 201 Washington Rd Princeton NJ 08543	
8. PERFORMING ORGANIZATION REPORT NUMBER N/A				9. SPONSORING/MONITORING AGENCY NAME(S) AND ADDRESS(ES) Advanced Research Projects Agency 3701 North Fairfax Drive Arlington VA 22203-1714	
10. SPONSORING/MONITORING AGENCY REPORT NUMBER RL-TR-94-195				11. SUPPLEMENTARY NOTES *Authors are from the Oregon Institute of Science and Technology Rome Laboratory Project Engineer: Ernst K. Walge/OCPC/(315) 330-3147	
12a. DISTRIBUTION/AVAILABILITY STATEMENT Approved for public release; distribution unlimited.				12b. DISTRIBUTION CODE	
13. ABSTRACT (Maximum 200 words) This research describes a novel approach to semiconductor lasers capable of ultra-high speed modulation. This approach uses the interaction between elements in a coherent diode laser array that results in lateral mode locking. This method potentially allows narrow-band modulation at rates above the relaxation oscillation frequency of the lasers, thus removing a major impediment to ultra-high speed modulation. Linearized analysis of coupled laser rate equations shows that the array can be asymptotically stable for values of the coupling attainable with index-guided lasers. The small-signal responsivity for a two-element array, for 180° out-of-phase/modulation, extends far beyond the relaxation oscillation frequency when examining the optical output from a single element. Large-signal analysis using full rate equations were used to demonstrate schemes for utilizing these microwave frequency resonances for high-speed optical signal transmissions. It was shown that digital signals with bit rates many times the relaxation oscillation frequency could be transmitted. Using lasers with a 4-GHz relaxation oscillation frequency, it is theoretically shown that rates of > 25 Gb/s can be achieved. This scheme can also be used for encoding analog information using narrow band amplitude modulation. It was demonstrated that a 44 GHz carrier with a 1-GHz amplitude modulated envelope signal could be (see reverse)					
14. SUBJECT TERMS Semiconductor lasers, Ultra-high speed modulation, Relaxation oscillation				15. NUMBER OF PAGES 60	
				16. PRICE CODE	
17. SECURITY CLASSIFICATION OF REPORT UNCLASSIFIED		18. SECURITY CLASSIFICATION OF THIS PAGE UNCLASSIFIED		19. SECURITY CLASSIFICATION OF ABSTRACT UNCLASSIFIED	
				20. LIMITATION OF ABSTRACT UL	

TABLE OF CONTENTS

Section	Page
SUMMARY.....	1
A. INTRODUCTION	3
B. THEORETICAL CONSIDERATIONS	6
1. The Model	8
2. Large-Signal Responsivity.....	9
3. Modulation Signals.....	10
C. PROOF-OF-CONCEPT ARRAY DESIGN	14
1. Two-Element Design	14
2. Three Element Array.....	17
3. Electrode Design – Minimizing Parasitics.....	18
D. LASER ARRAY FABRICATION	20
1. Polyimide-Isolated Process.....	21
2. Air-Isolated Interconnect Process.....	24
3. Silicon Nitride Based Process.....	26
E. LASER ARRAY EVALUATION	29
1. Evaluation At Oregon Graduate Institute.....	29
Optical Inspection.....	29
Current/Voltage Measurement.....	29
Light/Current Measurement	29
Near-Field Measurement.....	30
Spectral Measurement.....	30
Time Averaged Temporal Measurements	31
2. Network Analyzer Based Test Setup	31
Preliminary Test Procedure.....	33
F. CONCLUSIONS.....	35
G. RECOMMENDATIONS	37
REFERENCES.....	39

LIST OF FIGURES

Figure		Page
1.	Frequency regimes for direct modulation, lateral mode locking, and longitudinal mode locking.	5
2.	Small-signal responsivity for in-phase and out-of-phase modulation when examining the optical output from a single element. In-phase modulation curve identical to single semiconductor laser, displaying relaxation oscillation peak. Out-of-phase modulation allows wider bandwidth.....	7
3.	Large signal responsivity curves for $\alpha=1.0$ and 7.0 . Optimized couplings $\eta = 0.2 + j 0.003$ and $\eta = 0.2 + j 0.04$ respectively.....	10
4.	Optical time series (top) for an applied binary return-to-zero 010110111 signal at 25 Gb/s for $\alpha=7.0$ and $\eta=0.2 + j 0.04$. The two elements were biased at $3 \times I_{th}$. The antisymmetric drive signals used are shown in the bottom. Device parameters are as per Table 1.....	12
5.	Optical time series for a 1-GHz sinusoidal envelope on a 44-GHz sub-carrier modulated drive signal.....	13
6.	Schematic diagram of two-element array with typical dimensions. Note that the pn junction beyond the array is etched off to decrease capacitance and allow high-frequency modulation. Cavity length is $300 \mu\text{m}$	14
7.	Calculated real and imaginary parts of the coupling parameter for several effective index steps versus center-to-center space for two-element array.....	16
8.	Real and imaginary parts of the coupling parameter, η , for a 3-ridge array (center-to-center spacing = $5 \mu\text{m}$) versus gain in the center stripe normalized to gain in the outer ridges.....	18
9.	Electrode structure (anticipating discussion in next section) and associated capacitance calculated by parallel plate approximation (Not to scale.).....	19
10.	Top view of 3-stripe array. Letters A to J locate the regions corresponding to the cross-sections shown in Fig. 11.....	22
11a.	General cross-section showing keys to interpret Figs. 11b and 11c.....	22
11 b.	Cross-sections at points A to D identified in Fig. 10.....	23
11 c.	Cross-sections at points F to J identified in Fig. 10.....	24

LIST OF FIGURES (continued)

Figure		Page
12.	Air-isolated interconnect process.....	25
13.	Si ₃ N ₄ isolated process	27
14.	Schematic of test apparatus for lateral mode locked high speed laser.....	32
15.	Test schematic for network analyzer measurement.	33
16.	Degree of planarization (DOP)	37

LIST OF TABLES

Table		Page
1.	Semiconductor laser parameters used in coupled rate equation model. Values for single-quantum-well laser.....	7
2.	Laser array design goals.	20
3.	Wafer parameters.	21

SUMMARY

This report describes a concept validation study of a novel approach to the development of lasers capable of ultra-high-speed (> 30 GHz) modulation. This approach, developed by Professor Richard DeFrees and his co-workers at Oregon Graduate Institute (OGI), is based on the interaction between laser elements in a coherent semiconductor diode laser array that results in lateral mode locking. This method has the potential of allowing narrow-band modulation at rates above the relaxation oscillation frequency of the lasers, thus removing a major impediment to ultra-high-speed modulation.

Rate equation theory predicts that inter-element coupling in semiconductor laser arrays introduces new time constants into the laser's dynamical system. This phenomenon is related to the beating between *lateral* array modes and takes place at frequencies from 10 to 50 GHz for typical array designs employing index-guided laser elements.

Linearized analysis of coupled laser rate equations has shown that the array system can be asymptotically stable for values of the coupling attainable with practical index-guided lasers. The small-signal responsivity for a two-element array, for 180° out-of-phase (anti-symmetric) modulation, extends far beyond the relaxation oscillation frequency *when examining the optical output from a single element*.

A large signal analysis based on full rate equation theory is used to demonstrate schemes for utilizing these microwave frequency resonances for high-speed optical signal transmission. We show that digital signals with bit rates many times the relaxation oscillation frequency can be transmitted. The width of the inter-element responsivity resonance can also be exploited for encoding analog information using narrow band amplitude modulation (sub-carrier multiplexing - SCM).

To utilize the inter-element time constants for communications applications while suppressing relaxation oscillations, the coupled system must be maintained at dynamical equilibrium. The high-speed transfer of energy between array elements is stimulated by fast anti-symmetric drive level changes, but the original equilibrium must then be quickly restored otherwise the system begins to relax towards a new equilibrium and experiences relaxation oscillations. Digital signals should therefore be implemented in a return-to-zero (RZ) or similar scheme where the drive signal regularly returns to the original bias condition.

We considered the case of a 0101101110 RZ digital pattern, and our computations show that it can be implemented at *a bit rate of 25 Gbps. The relaxation oscillation frequency for the lasers in this two-element array is nominally 4 GHz.*

This phenomenon can also be exploited for encoding analog information using narrow-band amplitude modulation. We show that a 44 GHz carrier with a 1-GHz amplitude modulated envelope signal can be successfully implemented (same device parameters as used for the digital example).

Two- and three-element strained InGaAs/AlGaAs single-quantum-well laser arrays were designed. The lasers in these arrays were of a ridge waveguide geometry. The key device design and fabrication task was to design and implement a low parasitic electrode structure. The three-element array requires cross-overs for the electrodes and is thus more complicated. Process architectures for the fabrication of these arrays were generated and process development was begun.

The digital and analog results described are ad hoc examples and do not represent performance limits. Further study is recommended to optimize the array and quantify the performance capabilities and limitations. Other performance parameters that are of interest for microwave systems such as noise figure, linearity, and spur-free dynamic range must be studied both theoretically and experimentally. Processes for the high-yield fabrication of low-parasitic laser arrays must be developed to realize optical sources with high modulation capability.

A. INTRODUCTION

The objective of this program is to carry out a concept validation study of a novel approach to the development of lasers capable of ultra-high-speed (> 30 GHz) modulation. This approach, developed by Professor Richard DeFrez and his co-workers at Oregon Graduate Institute (OGI), is based on the interaction between laser elements in a coherent semiconductor diode laser array that results in lateral mode locking. This method has the potential of allowing narrow-band modulation at rates above the relaxation oscillation frequency of the lasers, thus removing a major impediment to ultra-high-speed modulation.

This program is a joint effort between Sarnoff (Prime Contractor) and OGI. The program responsibilities are as follows:

- Sarnoff: Program Management, Low-Parasitic Interconnect Design, Process Development, Laser Array Fabrication, and Network Analyzer Testing.
- OGI: Theory, Optical Design, and Streak Camera Testing

A major application of high-speed lasers is in military and commercial microwave systems. In microwave systems, it is necessary to generate, manipulate, and transport signals throughout the system. A well-known microwave system in which signal transportation plays a major role is a phased-array radar. Here, thousands of individual array elements must be controlled and appropriately phased for satisfactory operation. An optical fiber link is an excellent medium for this application for the obvious reasons of wide bandwidth, immunity to RFI, resistance to jamming, and low weight. To use an optical fiber, it is necessary to impose the microwave (and the digital control signals) on an optical carrier. Direct modulation of semiconductor diode lasers and the use of external modulators are two possible methods. In addition to transporting microwave and control signals, fiber links can also be used to provide phase shifts (and true time delays) for beamforming in phased array radars.

Present experimental strained-layer multi-quantum-well lasers have direct modulation bandwidths in the 20- to 30-GHz range (determined by the relaxation oscillation frequency) and may be adequate for many applications. However the relative intensity noise (RIN) of such lasers tends to mimic the modulation responsivity characteristic and peaks at the relaxation oscillation frequency. In practical systems, it is therefore necessary to operate well below the relaxation oscillation frequency. Furthermore, semiconductor lasers have to be run at their highest power levels to achieve the largest modulation bandwidth. Traveling wave external modulators can have

3-dB bandwidths in excess of 40 GHz, however they require a high drive voltage and have high optical insertion loss. Thus new methods to extend the modulation bandwidth of semiconductor lasers are required.

Many such microwave systems operate in a relatively narrow bandwidth at frequencies above the useful direct modulation bandwidth of semiconductor lasers. Methods for efficient and low noise, narrowband optical modulation above the direct modulation bandwidth will thus find use in such applications.

It was shown by Lau [1] that locking of the longitudinal modes of a semiconductor laser can result in narrow-band modulation at frequencies approaching 100 GHz. The relatively close spacing of the longitudinal modes prevents obtaining modulation at the more useful frequencies lying between 20 and 60 GHz. Recently, several investigators have resonantly enhanced the modulation bandwidth of semiconductor lasers near the relaxation oscillation frequency by appropriately using reactive circuit elements [2]. This also enhances the RIN [2] and suffers from the same disadvantage as direct modulation.

It has been shown that rate equation theory predicts that inter-element coupling in semiconductor laser arrays introduces new time constants into the laser's dynamical system [3]. This phenomenon is related to the beating between *lateral* array modes and takes place at frequencies from 10 to 50 GHz for typical array designs employing index-guided laser elements.

Linearized rate equation analysis has previously shown small-signal modulation resonances at these frequencies. We will use the full rate equation theory for large signal analysis and theoretically demonstrate potential schemes for utilizing these microwave frequency resonances for high-speed optical signal transmission. Figure 1 illustrates the frequency regimes for direct modulation, longitudinal mode locking, and lateral mode locking.

We will show that digital signals with bit rates many times the relaxation oscillation frequency can be transmitted. The width of the inter-element responsivity resonance can also be exploited for encoding analog information using narrow band amplitude modulation (sub-carrier multiplexing - SCM).

Preliminary efforts at fabrication of low parasitic laser arrays to demonstrate proof-of-concept are also described. It was not possible to achieve our experimental design goals within the time and budget constraints of the program. The results obtained to date are encouraging and are described in detail. The potential benefits of carrying out this effort are summarized below:

- Modulation at frequencies $>$ relaxation oscillation frequency (direct modulation limit)
- Enable transmission of millimeter-wave signals over optical fiber for:
 - Phased-array radar

- Subcarrier multiplexing for communications
- Multistatic radar
- Beamforming for radars

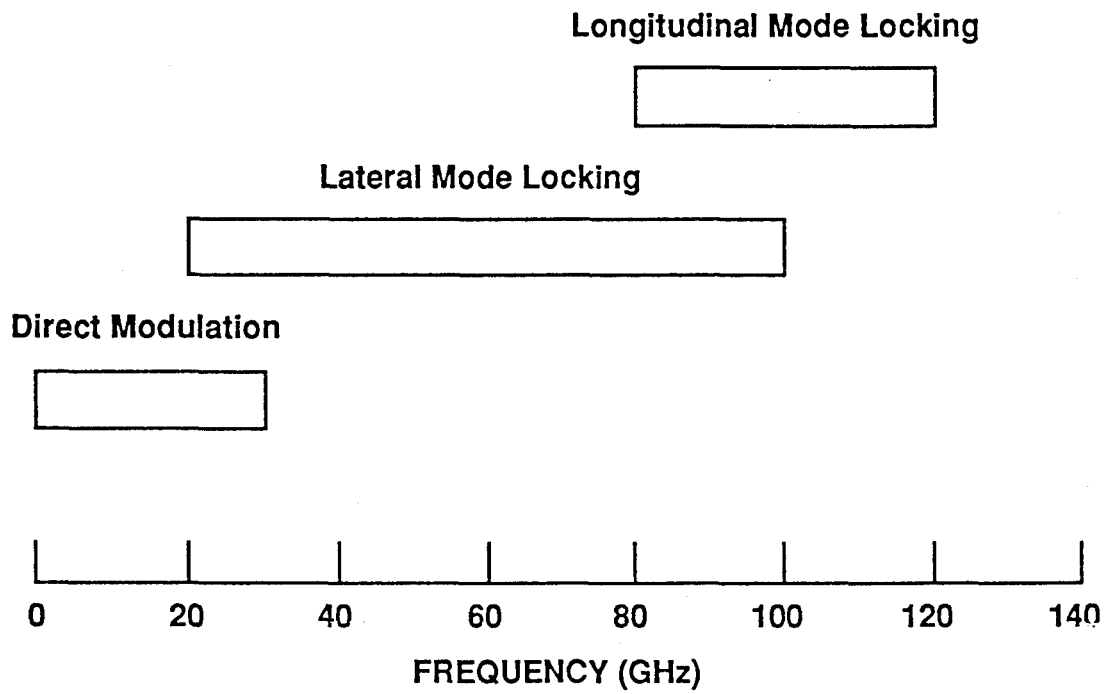


Figure 1. Frequency regimes for direct modulation, lateral mode locking, and longitudinal mode locking.

B. THEORETICAL CONSIDERATIONS

Rate equation theory predicts that inter-element coupling in semiconductor laser arrays introduces new time constants into the laser's dynamical system. This phenomenon is related to the beating between *lateral* array modes and takes place at frequencies from 10 to 50 GHz for typical array designs employing index-guided laser elements. Previous analyses using the linearized rate equations have shown that small-signal modulation resonances occur at these frequencies. We have used the full rate equation theory for large signal analysis and theoretically demonstrate potential schemes for utilizing these microwave frequency resonances for high-speed optical signal transmission. We show that digital signals with bit rates many times the relaxation oscillation frequency can be transmitted. The width of the inter-element responsivity resonance can also be exploited for encoding analog information using narrow band amplitude modulation (sub-carrier multiplexing - SCM).

Semiconductor laser arrays have received considerable attention as potentially high-power, high-efficiency coherent optical sources. However, high-speed experimental studies of these arrays have frequently found complex nonlinear dynamics including self-pulsing, quasi-periodic, and erratic behaviors [3]. In addition, these observations have revealed time constants that are shorter than the relaxation time but longer than the round trip time of the laser cavity. These microwave frequency behaviors have been attributed to interactions between array elements [4, 5] and typically span from 10 to 50 GHz for index-guided laser structures [6, 7].

Linearized analysis [6, 7] of a dynamical model based on coupled laser rate equations has shown that the array system can be asymptotically stable for values of the coupling attainable with practical index-guided lasers. It was also found that the energy exchange between elements resonates at the inter-element time constant and is strongly promoted when the two laser elements are subjected to anti-symmetric (180° out-of-phase) modulation.

Figure 2 shows the small-signal responsivity for both in-phase (symmetric) and out-of-phase (anti-symmetric) modulation *when examining the optical output from a single element*. The model parameters are listed in Table 1. The inter-element coupling coefficient, η , is equal to $0.2+j0.04$ and the linewidth enhancement factor, α , is 7. Spontaneous emission and nonlinear gain are ignored in the linearized analysis. The in-phase modulation curve is identical to that of a single semiconductor laser, displaying a relaxation oscillation peak near 4 GHz. Anti-symmetric modulation, on the other hand, produces a resonance peak at the inter-element coupling time but the relaxation oscillation has disappeared because the total energy of the system, and the total optical output summed over the two emitters, remains nearly constant; energy is rapidly transferred between elements, while the carrier-photon dynamic equilibrium for the entire array is essentially

unchanged. The high frequency inter-element resonance shown in the Fig. 2 allows microwave optical modulation and bypasses many of the limitations associated with semiconductor laser designs based on a high relaxation oscillation frequency.

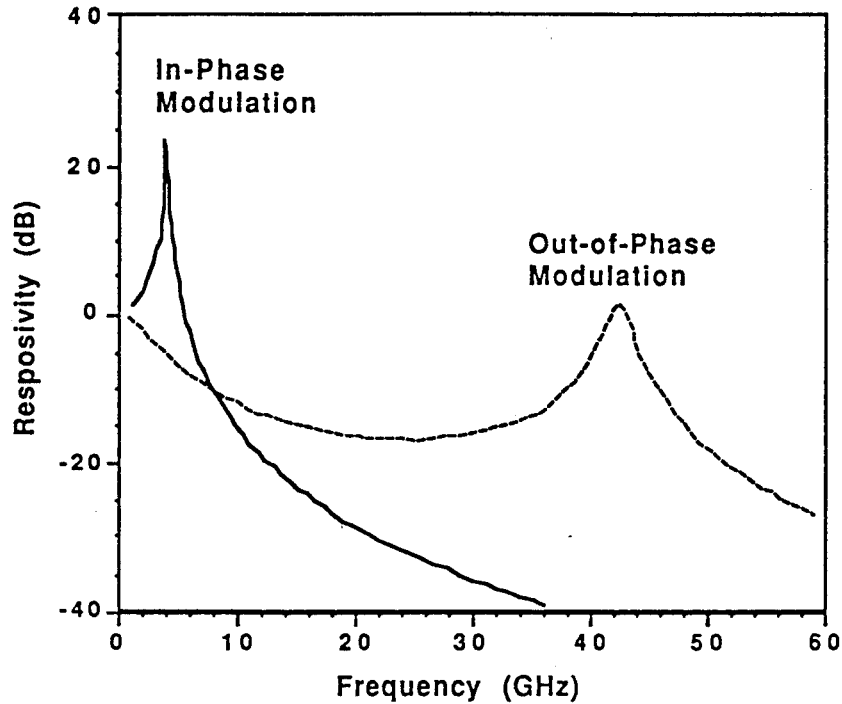


Figure 2. Small-signal responsivity for in-phase and out-of-phase modulation when examining the optical output from a single element. In-phase modulation curve identical to that of single semiconductor laser, displaying relaxation oscillation peak. Out-of-phase modulation allows much wider responsivity bandwidth.

Table 1. Semiconductor laser parameters used in coupled rate equation model. Values for single-quantum-well laser.

Parameter	Symbol	Value
Photon Lifetime	τ_p	1.5 ps
Carrier Lifetime	τ_c	2.4 ns
Differential Gain	$\frac{dG}{dN}$	$1 \times 10^{15} \text{ cm}^2$
Threshold Carrier Density	N_{th}	$9 \times 10^{18} \text{ cm}^{-3}$
Group Index	n_g	4.0
Confinement Factor	Γ	0.02

In sections B.1 and B.2, the rate equation analysis is extended using full nonlinear equations and numerical integration. Large signal responsivity is found to match small-signal calculations. Two schemes that utilize inter-element time constants for encoding high speed optical information are examined. *Numerical analysis shows that electrically modulated arrays can produce optical bit rates significantly higher than the relaxation oscillation frequency.*

1. The Model

The dynamical model used to investigate the effects of inter-element optical coupling on array dynamics is described in references [6, 7]. The model is derived from sets of standard nonlinear semiconductor laser rate equations coupled by a complex coupling parameter that represents nearest-neighbor evanescent field coupling. Each element is assumed to be identical and that it can support single transverse, lateral, and longitudinal modes. The ensemble of normalized rate equations for a two-element array takes the following form [5, 7]:

$$\begin{aligned}
 \dot{X}_1 &= \frac{1}{2}[k_1(1+2Z_1)-1]X_1 + \frac{B}{X_1} - X_2(\eta_r \sin \phi + \eta_i \cos \phi) \\
 \dot{X}_2 &= \frac{1}{2}[k_2(1+2Z_2)-1]X_2 + \frac{B}{X_2} + X_1(\eta_r \sin \phi - \eta_i \cos \phi) \\
 \dot{\phi} &= -\alpha(Z_2 - Z_1) + \eta_r \cos \phi \left(\frac{X_1}{X_2} - \frac{X_2}{X_1} \right) + \eta_i \sin \phi \left(\frac{X_1}{X_2} + \frac{X_2}{X_1} \right) \\
 T\dot{Z}_1 &= p_1 - Z_1 - k_1(1+2Z_1)X_1^2 \\
 T\dot{Z}_2 &= p_2 - k_2(1+2Z_2)X_2^2
 \end{aligned} \tag{1}$$

where X_j , Z_j and p_j are, respectively, the normalized field magnitude, gain, and pumping in each element. The optical phase difference between the two emitters is ϕ , T is the ratio of the carrier and photon lifetimes, α is the linewidth enhancement factor, η is the complex inter-element coupling coefficient, and B is the normalized spontaneous emission factor. Gain non-linearity is incorporated through the k_j 's, taken here in the form [8]

$$k_j^2 = \frac{1}{1 + \frac{X_j^2}{X_{sat}^2}} \tag{2}$$

The complex coupling coefficient η has its origins in coupled-mode theory [6, 7, 9] and is calculated from the overlap of the optical fields from adjacent elements. The real part of the coupling is approximately proportional to the rate of energy exchange between elements and the

frequency splitting of the lateral array modes. The imaginary part reflects the relative array mode threshold gains and influences stability by determining the dominant lateral array mode. These nearest neighbor coupled rate equations are considered valid when the optical modes in each element are well controlled and independent of drive level.

2. Large-Signal Responsivity

Examination of higher order terms in the linearized small-signal analysis might yield information concerning the validity of small-signal modulation response with respect to drive signals of non-infinitesimal magnitude. However, such a higher-order analytical calculation is difficult, inflexible, and provides only limited qualitative insight. Instead, we determine large-signal responsivity of the two-element array using a generalized numerical method to allow convenient transition to arbitrary drive signals.

A large signal sinusoid was anti-symmetrically applied through drive terms (p_i) in the full nonlinear rate equations, Eq.(1), and the system was numerically integrated until a stable optical limit cycle was found at the applied signal frequency. The magnitude and phase of the modulated limit cycle were then measured by least squares fitting a sinusoid to the optical time series. This procedure was repeated, incrementing through a range of frequencies, and a responsivity curve was obtained.

Figure 3 shows the out-of-phase, large-signal-modulation response for an array (with the same parameters as used in Fig. 1) for linewidth enhancement factors of 1.0 and 7.0. The array is biased at $2 \times I_{th}$, and the drive modulation signal oscillates from $1.1 \times I_{th}$ to $2.9 \times I_{th}$. The large-signal responsivity is very similar to the linearized out-of-phase small-signal results shown in Fig. 1 for $\alpha=7.0$. The "glitch" in the curve near the relaxation oscillation frequency is due to nonlinear distortion of the optical limit cycle away from a sinusoid.

An interesting behavior of this coupled rate equation system is the dependence of the responsivity upon the linewidth enhancement factor. The value of α strongly affects the width and height of the out-of-phase resonances as shown in Fig. 3. Note that the two examples also have different imaginary coupling parameter values to maintain maximum peak responsivity. These results suggest that high linewidth enhancement factor devices are preferable due to their flatter broadband responsivity curves. However, high α arrays are also more susceptible to inherent instabilities that restrict the available range of stable coupling values.

The spontaneous emission factor and gain compression were ignored in this calculation because their inclusion provides only a small additional damping to the system. The primary nonlinearities in equations, Eq.(1), are the gain/field and adjacent-element field/phase interactions. When either spontaneous emission or gain non-linearity is included, using typical values associated

with index guided lasers, the only effect is a slight decrease in the maximum modulation response of both the relaxation oscillation and the out-of-phase modulation resonances.

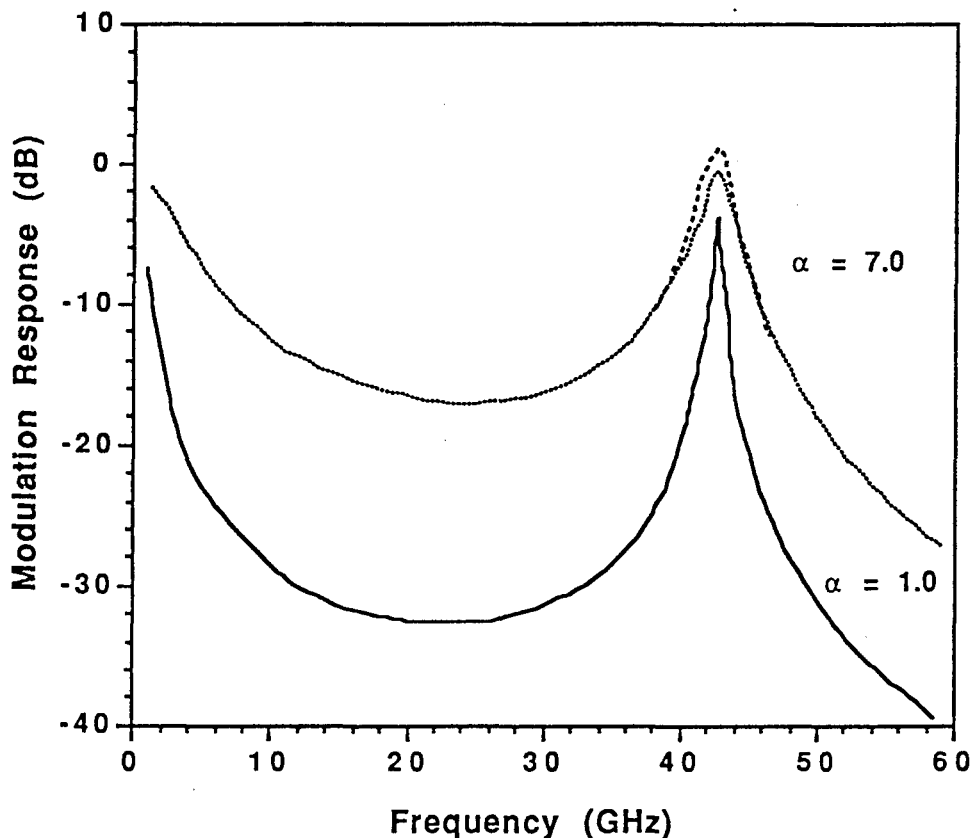


Figure 3. Large signal responsivity curves for $\alpha=1.0$ and 7.0 . Optimized couplings $\eta = 0.2 + j0.003$ and $\eta = 0.2 + j0.04$ respectively. Device parameters in Table 1; drive signal oscillated from $1.1 \times I_{th}$ to $2.9 \times I_{th}$. Dashed line is renormalized out-of-phase small-signal modulation curve from Fig. 1 for comparison.

3. Modulation Signals

To utilize the inter-element time constants for communications applications while suppressing relaxation oscillations, the coupled system must be maintained at dynamical equilibrium. The high-speed transfer of energy between elements is stimulated by fast anti-symmetric drive level changes, but the original equilibrium must then be quickly restored otherwise the system begins to relax towards a new equilibrium and experiences relaxation oscillations. The appropriate type of binary signal must be chosen to ensure that the equilibrium is regularly enforced for arbitrary bit patterns. With an anti-symmetric Non-Return-to-Zero (NRZ) encoding

scheme, a series of binary 1's could result in periods of asymmetric drive levels sufficiently long for the system to relax towards a new asymmetric equilibrium. Digital signals should therefore be implemented in a return-to-zero (RZ) or similar scheme where the drive signal regularly returns to the original bias condition.

Figure 4 shows the optical output of the integrated rate equations for a 0101101110 RZ digital pattern at a bit rate of 25 Gb/s. The linewidth enhancement factor was taken as 7.0, the optimized coupling value was $\eta = 0.2 + j 0.04$. As shown in the Fig. 4, the signal is conditioned by the addition of an overshoot on the return transition to ensure a fast return to the initial dynamic equilibrium. *The relaxation oscillation frequency for this device is nominally 4 GHz.*

The width of the inter-element responsivity resonance can also be exploited for encoding analog information using narrow-band amplitude modulation (sub-carrier multiplexing - SCM). Figure 5 shows the integrated rate equation time series for a 44 GHz carrier with a 1-GHz amplitude modulated envelope signal for the same device parameters used previously with $\alpha=7.0$ and η (after optimization) = $0.2 + j 0.04$. SCM can be used in many military system such as multi-static radars, carrying control and signal information to the elements of a phased array, etc.

In summary, rate equation theory predicts that the high speed inter-element energy exchange in two-element semiconductor laser arrays can be exploited for high speed optical modulation with signals of arbitrarily large magnitudes. This has been demonstrated in principle for both digital and AM analog signals. However, the total energy contained in the dynamical system must be maintained in an equilibrium state leading to an optical bias on the output intensity level. This optical bias can be eliminated electronically at the receiver, or by coherent manipulation of the optical output of the two elements. It is found that the value of the linewidth enhancement factor significantly affects the shape of the frequency responsivity curve with larger values providing a wider inter-element response resonance. The value of the coupling parameter is critical in balancing the optimum response with dynamical damping and stability.

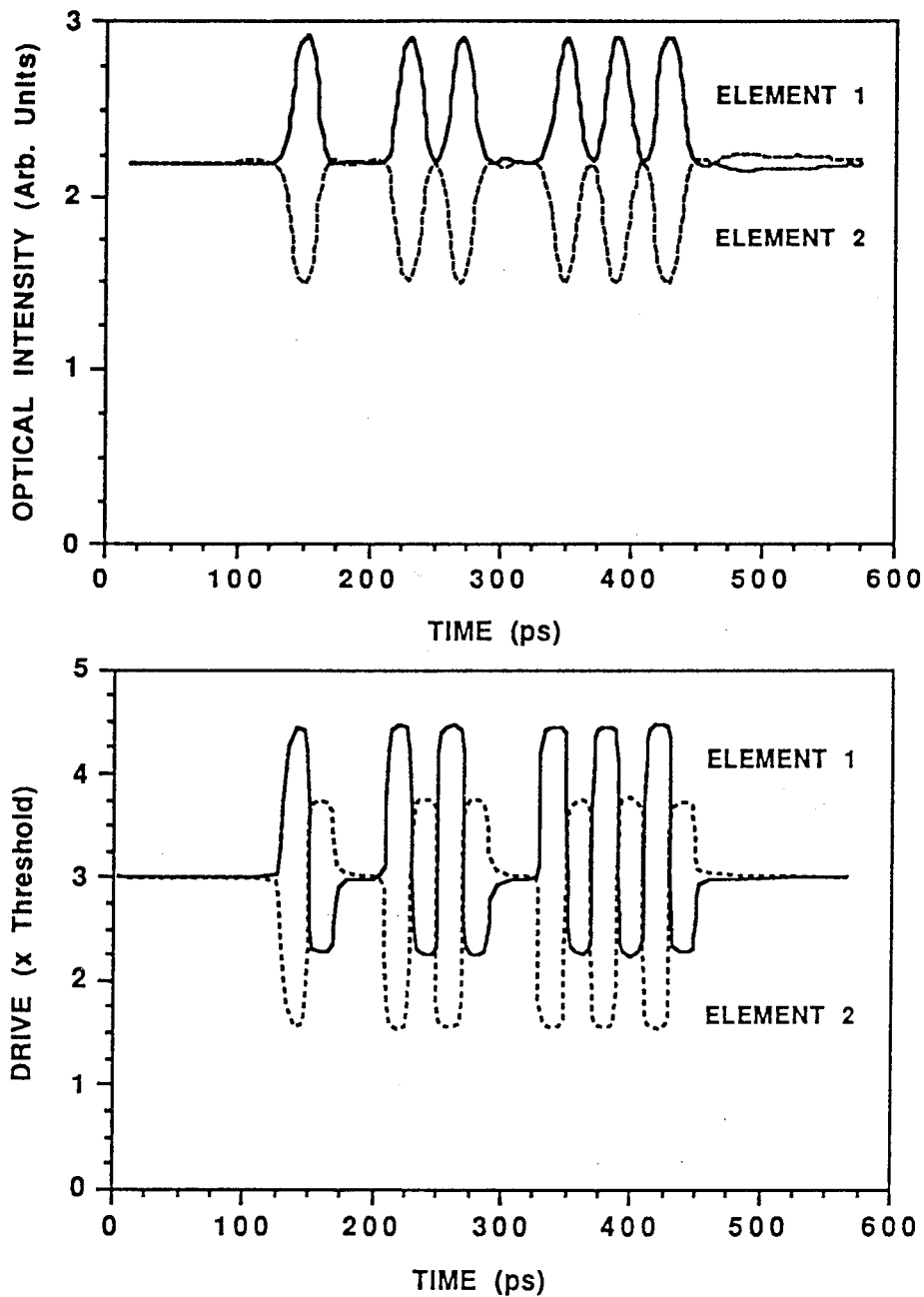


Figure 4. Optical time series (top) for an applied binary return-to-zero 010110111 signal at 25 Gbls for $\alpha=7.0$ and $\eta=0.2 + j0.04$. The two elements were biased at $3 \times I_{th}$. The antisymmetric drive signals used are shown in the bottom. Device parameters are as per Table 1.

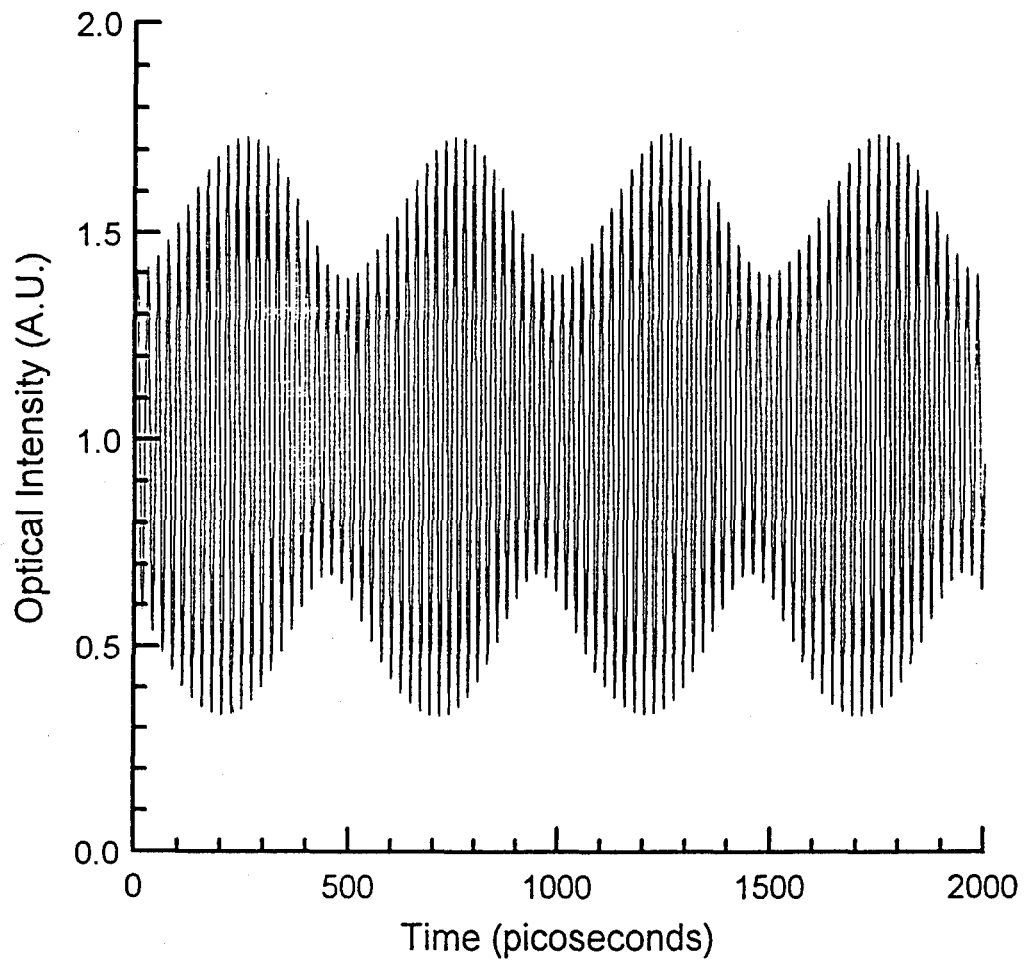


Figure 5. Optical time series for a 1-GHz sinusoidal envelope on a 44-GHz sub-carrier modulated drive signal.

C. PROOF-OF-CONCEPT ARRAY DESIGN

1. Two-Element Design

Figure 6 shows the 2.5- μm -wide by 300- μm -long ridge waveguide stripe structure designed for this project. The array element is similar to the ridge waveguide laser structures extensively fabricated at Sarnoff. The material parameters are for a typical strained InGaAs single-quantum-well laser. The p-cladding is 1.3- μm thick under the ridges. Between the ridges, the p-cladding will be etched down to 0.15- μm thickness. The built-in effective index step for this design is 0.0045. Estimating the p-cladding resistivity to be $4 \times 10^{-2} \Omega \text{ cm}$, the isolation between emitters is 35Ω for stripes 4- μm apart and larger for greater separations.

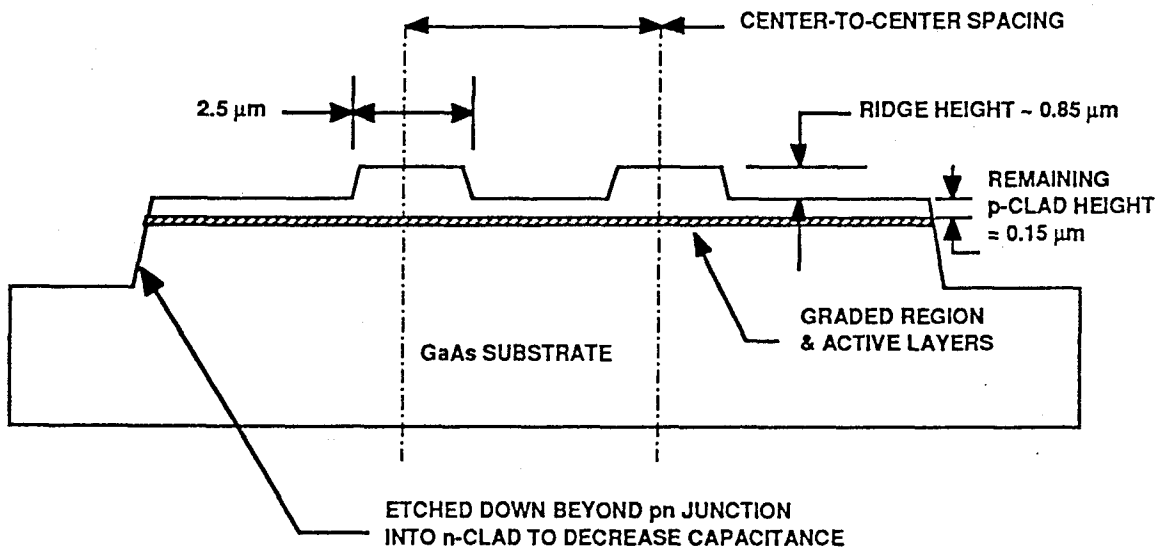


Figure 6. Schematic diagram of two-element array with typical dimensions. Note that the pn junction beyond the array is etched off to decrease capacitance and allow high-frequency modulation. Cavity length is 300 μm .

Calculations of the emitter coupling parameter involve comparison of the complex propagation values of the two-element lateral modes to those obtained from a single emitter of the same ridge structure. The modal eigenvalues for different index steps and emitter separation were calculated using the effective index method and a complex layered waveguide eigenvalue solver. The general expression for the complex coupling parameter is:

$$\tilde{\eta} = \frac{\tau_p c}{2} (\tilde{k}_+ - \tilde{k}_-) \quad (3)$$

where τ_p is the photon lifetime, and the k 's are the complex modal propagation constants. η_r , derived from the modal frequency splitting (real part of k), is then:

$$\eta_r = \frac{\tau_p}{2}(\omega_+ - \omega_-) = \frac{\tau_p \omega_0 n_{r,0}}{2} \left(\frac{1}{n_{r,+}} - \frac{1}{n_{r,-}} \right) \quad (4)$$

where the n_r 's are the real parts of the calculated effective indices of the three modes and the ω 's are their frequencies. The corresponding expression for η_i (imaginary part) is:

$$\eta_i = \frac{\tau_p \omega_0}{2n_{r,0}} (n_{i,-} - n_{i,+}) \quad (5)$$

where the n_i 's are the imaginary parts of the effective indices. The non-zero imaginary effective index components result from the addition of a complex effective index step under the ridges. The imaginary effective index step, corresponding to gain, was chosen to be on the order of the mirror loss in an uncoated 300- μm -long cavity. If the real index steps are sufficiently large to dominate lateral waveguiding, the magnitude of the imaginary step is only of minor importance to the calculated splitting of the real effective index. For example, in the case of a ridge real index step of 0.004, doubling the complex step affected the real modal splitting by <1 percent, while almost doubling the imaginary splitting. The case of pure gain guiding is more complicated.

The calculated coupling constants for different real index steps are shown in Fig. 7. The results of pure gain-guided coupling calculations are significantly larger than calculations with even small index guiding. Experimentally, albeit with a different device structure, a coupling parameter of $0.3 - j 0.4$ has been measured in a gain-guided, two-element device [4] and this compares favorably with the values obtained in these calculations.

Carrier effects such as carrier concentration induced index shifts and diffusion were not explicitly considered. These effects were added, in an ad hoc manner, as adjustments to the real and complex layer indices to improve the calculations. Index reductions in the InGaAs QW due to the threshold carrier concentration is estimated to be -0.04 when using the parameters in Table 1 and a threshold current of around 10 mA ($\sim 2 \times 10^{19}$ carriers/cm³). The associated transverse effective index decrease is about 0.002. As demonstrated by the difference of the 0.004 and 0.002 index step traces shown in Fig. 7, this index step reduction increases the coupling constant.

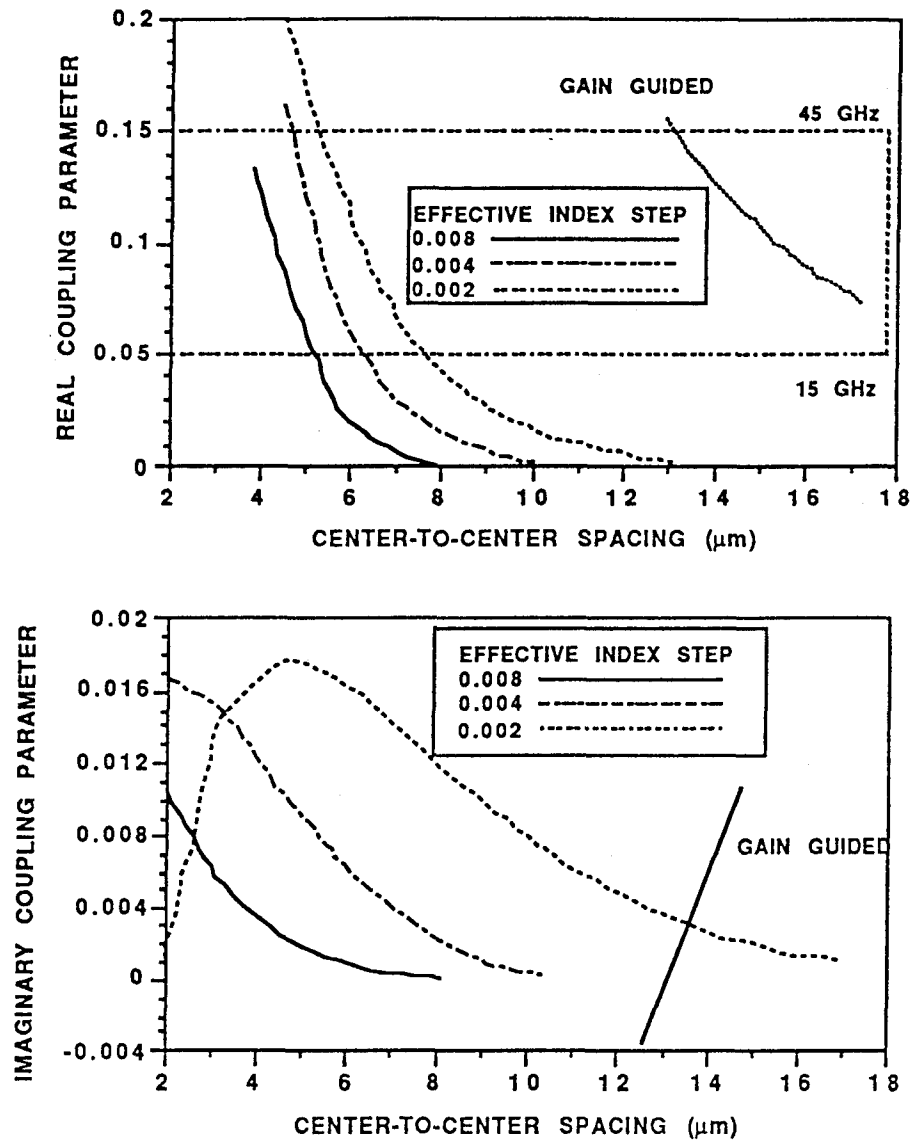


Figure 7. Calculated real and imaginary parts of the coupling parameter for several effective index steps versus center-to-center space for two-element array.

Carrier spreading in the active layer due to the high carrier diffusion coefficient acts to decrease loss (or increases gain) and to depress the index between the stripes. Changing the imaginary index between stripes only slightly affects the real part of the coupling provided, that the real index step under the ridges is of sufficient size to dominate waveguiding. For the case of a real index step of 0.004, the changes in coupling between when there is zero gain between the ridges, and when there is the same gain between the ridges as under the ridges, is <1 percent for η_r . However, the imaginary component changes considerably because the in-phase mode can utilize the increased gain between the stripes much more efficiently than the out-of-phase mode.

The carrier induced real index reduction between stripes decreases coupling whereas the same effect under the ridges increases coupling. The ridges provide an index step sufficient (0.004-0.008) to maintain adequate index guiding with a reasonable safety margin.

It was decided to etch below the p-n junction into the n-clad layer several micrometers away from the array in order to decrease p-n junction capacitance. This will not affect the coupling parameter unless the etch comes relatively close to the ridges. For an index step of 0.0045, a distance of 3 μm between the edge of the ridge and the second etch has negligible effects upon the coupling parameter. For an index step around 0.002, as the InGaAs material would experience during operation, it is necessary to maintain a larger distance of around 5 μm .

The center-to-center spacing chosen to ensure a good range of coupling parameter values are 4, 5, 6, 8, 10 and 15 μm . Due to the smaller index step of the InGaAs wafer structure, and the corresponding increased coupling, the spacing of 5 to 6 μm will probably be the most successful at approaching the desired goal of $\eta_r = 0.1$ and 30 GHz modulation. The larger spacings were provided as a safety margin. The larger separations may also prove more experimentally tractable for proof-of-concept demonstration at frequencies <30 GHz. A single mask with these spacings will cover an adequate range of coupling parameter magnitudes. The isolation between emitters of this design range from 35 to 115 Ω for emitter separations of 4 to 15 μm .

In summary, after a complex eigenmode analysis of two-element arrays fabricated from InGaAs SQW material, center-to-center spacings for the ridges of 4, 5, 6, 8, 10, and 15 μm were chosen. A center-to-center spacing of 5 μm was chosen for the three-element array.

2. Three Element Array

A three-element device can be used as a variable coupling two-element array. The third contact is located between the two elements and can be biased to vary the coupling between the two outer elements by carrier induced gain and index shifts. The structure is identical to two-element devices but with three ridges and the interconnect pattern will require cross-overs. The chosen center-to-center spacing is 5 μm .

Figure 8 shows the calculated coupling parameters vs the gain in the center element for the case of a three-ridge array with a real index step of 0.004. When the gain under the center ridge is greater than about half that of the outer two ridges, the near field diverges from the conventional two-element shape and begins to behave like a three-element array. There appears to be an adequate tuning range of center stripe gain values below the two- to three-element array transition point to observe a roughly factor of 2 increase in coupling. The 5- μm spacing value results from a balance between the nominal real coupling when the center emitter is unpumped, and the transition to a three-element array.

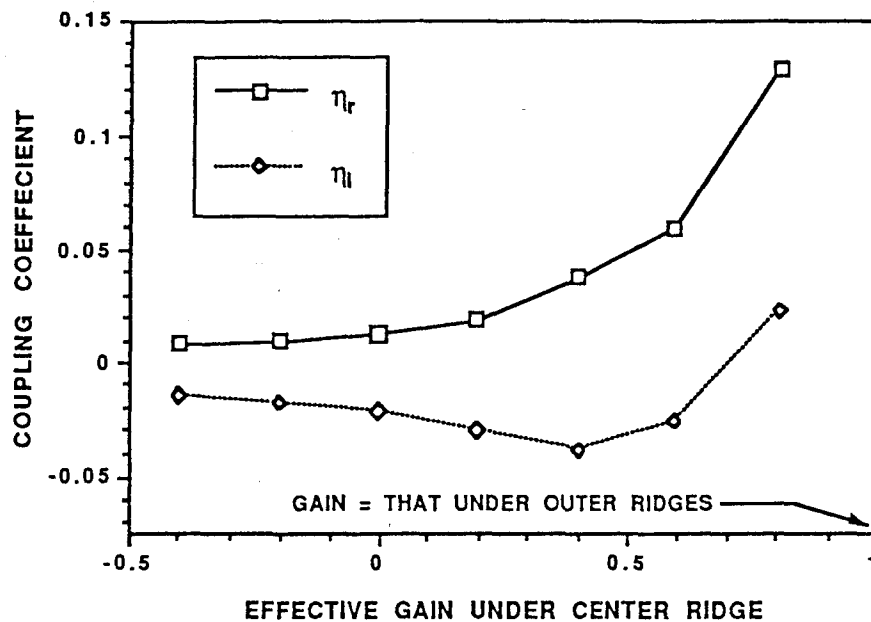


Figure 8. Real and imaginary parts of the coupling parameter, η , for a 3-ridge array (center-to-center spacing = $5 \mu\text{m}$) vs gain in the center stripe normalized to gain in the outer ridges.

3. Electrode Design – Minimizing Parasitics

It is necessary to ensure that the parasitic reactances associated with the electrode structure and the laser epilayers be minimized so that high-speed modulation can be obtained. It is the *extrinsic* performance that will make such arrays practical; it is not enough to design an array with high-speed *intrinsic* performance. As discussed in the previous section, the p-n-junction epilayers outside the devices will be etched away everywhere to within a distance equal to twice the ridge separation. This will reduce the parasitic capacitance without perturbing the optical waveguide characteristics of the laser.

Designing a minimum parasitic electrode configuration requires a trade-off between many conflicting requirements. The electrodes must be capable of carrying the device current. In practical devices the current density is also subject to an electromigration constraint to ensure long operating life. Other constraints are set by the fabrication processes used. It should be noted that very stringent requirements can lead to unacceptably low device yields.

The criteria for electrode design are:

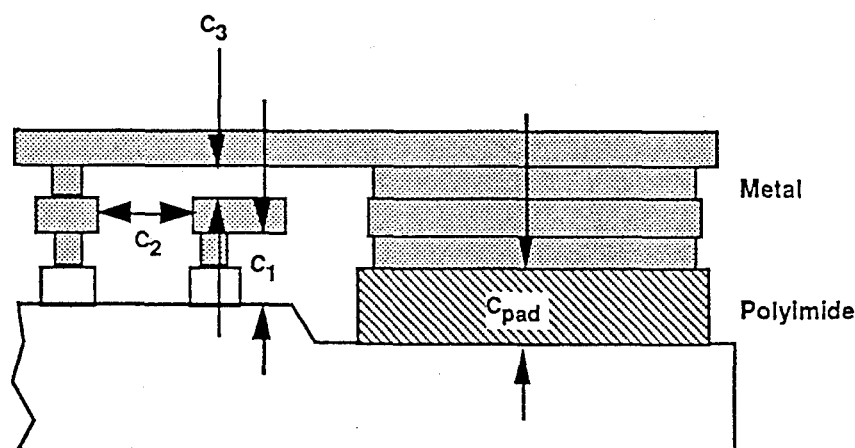
- Minimum possible capacitance.

- Cross-section sufficiently large to ensure current density is lower than the electromigration limit ($\leq 6 \text{ mA}/\mu\text{m}^2$ for Au).
- Compatible with standard edge-emitting laser fabrication process.
- Compatible with standard cleaving/chipping procedure to obtain good yield.
- Three-ridge array requires cross-overs.

The total parasitic reactances for our preliminary design were estimated as given below. This anticipates some of the fabrication related discussion presented in the next section but is given here for completeness.

The differential series resistance and the junction capacitance associated with the array have been calculated. Under forward bias, the junction capacitance of the InGaAs SQW-GRINSCH structure (nominal wavelength $\sim 950 \text{ nm}$) is estimated to be about 1 pF . The differential resistance of the $2.5\text{-}\mu\text{m}$ -wide ridge guide is estimated to be about 20Ω . The frequency roll-off due to the junction capacitance thus occurs at about 50 GHz . Since we are employing a graded confinement layer (GRINSCH), there is a built-in electric field that will reduce carrier transit times and the associated modulation damping effects that have been observed in InGaAs/GaAs SCH lasers.

The added capacitance due to the electrode structure (Fig. 9) is estimated to be $\sim 0.3 \text{ pF}$. (Calculated using the parallel-plate approximation.) The present design is therefore more than adequate to support the planned 25 GHz lateral-mode locked operation of these devices.



C ₁	Electrode to n+ Layer	$\sim 0.06 \text{ pF}$
C ₂	Electrode to adjacent electrode	$\sim 0.02 \text{ pF}$
C ₃	Cross-over ($20 \mu\text{m} \times 20 \mu\text{m}$)	$\sim 0.01 \text{ pF}$
C _{pad}	$40 \mu\text{m} \times 40 \mu\text{m}$ on Polyimide ($k = 3.5$)	$\sim 0.2 \text{ pF}$
Total Electrode Capacitance		$\sim 0.3 \text{ pF}$

Figure 9. Electrode structure (anticipating discussion in next section) and associated capacitance calculated by parallel plate approximation (Not to scale.).

D. LASER ARRAY FABRICATION

The goals for the laser array chosen at the beginning of the program are shown in Table 2. The material specifications and device structure were based on a ridge waveguide, edge-emitting laser, previously developed at Sarnoff, with which we had extensive experience. The key device fabrication task was to develop a two- and three-element array with an associated low-parasitic-reactance interconnect structure. The baseline structure was the two-element array. A three-element array was also incorporated in the masks. The three-element array requires cross-overs for the electrodes. Table 2 summarizes the salient features of the materials and device structure, and Table 3 lists the wafer parameters.

Table 2. Laser array design goals.

Material Structure

- Strained-Quayer InGaAs/GaAs Single-Quantum Well
- $\lambda = 950 \text{ nm}$: Differential Gain = 10^{-15} cm^2 : $\alpha = 1$
- Carrier Lifetime = 2 ns: Photon Lifetime = $\sim 1.5 \text{ ps}$ (Measured at OGI on Similar Material)

Device Structure

- Ridge Width = $2.5 \mu\text{m}$
- Two-Ridge Array - Baseline Device
 - Center-to-Center Spacing: 4, 5, 6, 8, 10, & $15 \mu\text{m}$
- Three-Ridge Array – Center Ridge For Coupling Control (by DC Biasing)
 - Center-to-Center Spacing: $5 \mu\text{m}$
- Ridge Waveguide Length = $300 \mu\text{m}$

Electrode Design Criteria

- Minimum Parasitic Capacitance
- Electromigration Limit: Current $< 6 \text{ mA}/\mu\text{m}^2$
- Compatibility With Standard Processing including Cleaving

Based on these criteria, a polyimide-isolated device geometry was designed. This geometry is shown in Fig. 10. Figure 10 shows the most complex structure, the three-element unit. Note that the polyimide used for the interconnect has been removed from the chip periphery to allow cleaving. Additional pads are provided as bonding/soldering aids. The letters on the right of Fig. 10 serve as keys to Fig. 11, where the device cross-sections at various points on the chip

are shown. The chip size is 300 x 300 μm , the RF bond pads are 40 x 40 μm , and the polyimide stops 25 μm from the edges. The substrate thickness is 100 μm . The p- and n-ohmic metals are Ti/Pt/Au (80/120/200 nm deposited at 300°C), and Ge/Au/Ni/Au (23.5/47/30/100 nm deposited at 150°C, sintered at 450°C, followed by Ti/Au, 20/200 nm deposited at 150°C), respectively. The metalization thicknesses are a trade-off that allows easy cleaving and yet carries the required current density.

Table 3. Wafer parameters.

Layer	Material	Thickness (μm)	$ N_D - N_A $ (cm^{-3})	Dopant
p-Cap	GaAs	0.1	10^{18}	Zn
Transition	$\text{Al}_{1-x}\text{Ga}_x\text{As}$ $x = 0.7 \rightarrow 0.1$	0.1	10^{18}	Zn
p-Clad	$\text{Al}_{0.7}\text{Ga}_{0.3}\text{As}$	1.1	$1 \rightarrow 10^{17}$	
GRIN	$\text{Al}_{1-x}\text{Ga}_x\text{As}$ $x = 0.08 \rightarrow 0.7$	0.15	- Undoped	
Barrier	GaAs	0.01	- Undoped	
QW	$\text{In}_{0.15}\text{Ga}_{0.85}\text{As}$	0.007	- Undoped	
Barrier	GaAs	0.01	- Undoped	
GRIN	$\text{Al}_{1-x}\text{Ga}_x\text{As}$ $x = 0.7 \rightarrow 0.08$	0.15	- Undoped	
n-Clad	$\text{Al}_{0.7}\text{Ga}_{0.3}\text{As}$	1.1	$10 \rightarrow 10^{17}$	Si
Transition	$\text{Al}_{1-x}\text{Ga}_x\text{As}$ $x = 0.1 \rightarrow 0.7$	0.1	10^{18}	Si
Buffer	GaAs	0.02	10^{18}	Si
Substrate	GaAs		$1-4 \times 10^{18}$	Si

1. Polyimide-Isolated Process

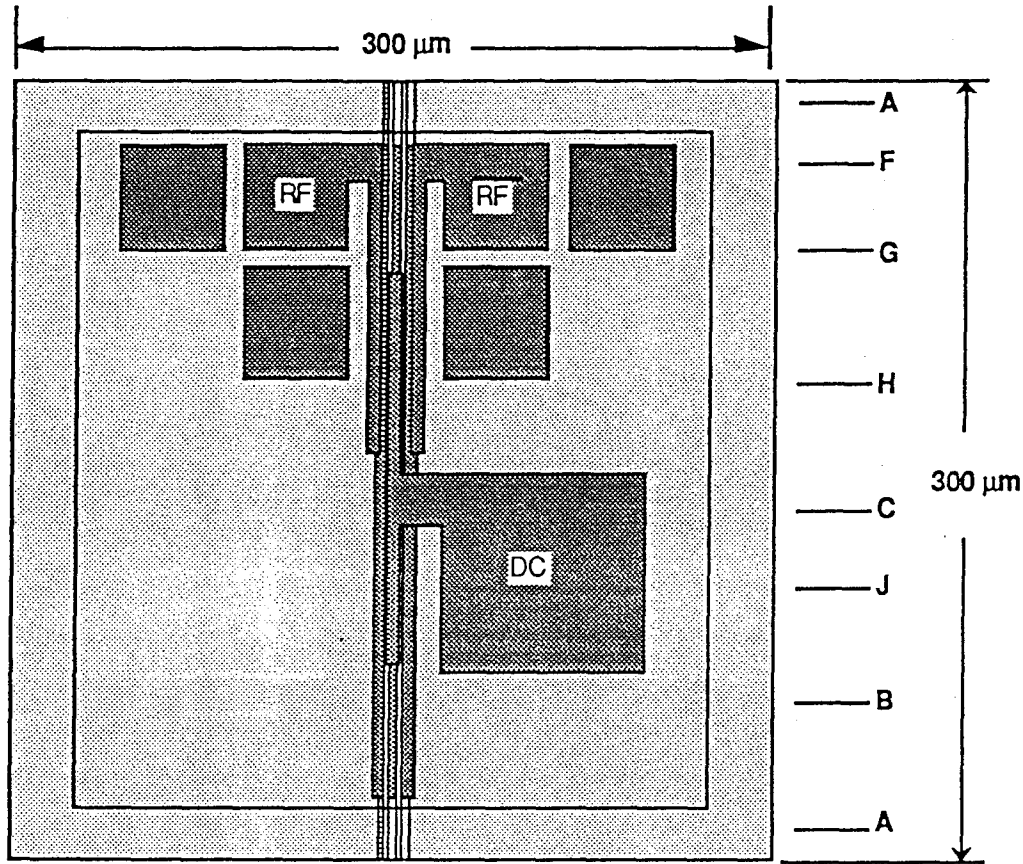
The first attempt at process development envisaged a complete polyimide-isolated structure as shown in Figs. 10 and 11. This was an aggressive approach aimed at producing the lowest parasitic structure. The features of this configuration are:

- Minimum parasitic capacitance design - Goal < 1 pF
- Thick (> 2 μm) Polyimide (Low ϵ) under 40- x 40- μm bond pads
- Polyimide-Isolated metal bridge interconnect from ~ 2.5- μm -wide ridges to bond pad

There were many processing problems, the chief among them being the following:

- Could not planarize polyimide over 2- μm -wide ridges
- Planarization not achieved even for 15- μm ridge separations
- Whole-wafer plasma etching attempted for planarization – No success
- Non-planarity prevented alignment and opening of apertures over ridge tops for interconnect post definition

Because of these problems, we attempted to develop an air-isolated interconnect process. The features of this process are: (a) polyimide-isolated bond pads and (b) air-isolated metal bridge interconnects. This is shown in Fig. 12.



40 μm x 40 μm RF pads and solder aids

Figure 10. Top view of 3-stripe array. Letters A to J locate the regions corresponding to the cross-sections shown in Fig. 11.

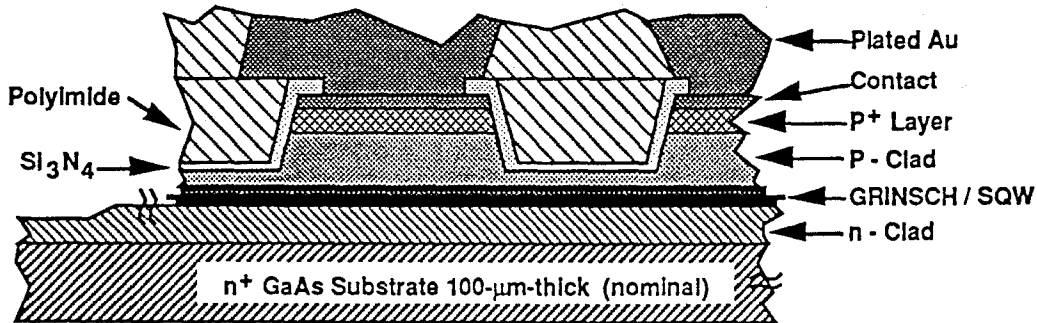


Figure 11a. General cross-section showing keys to interpret Figs. 11b and 11c.

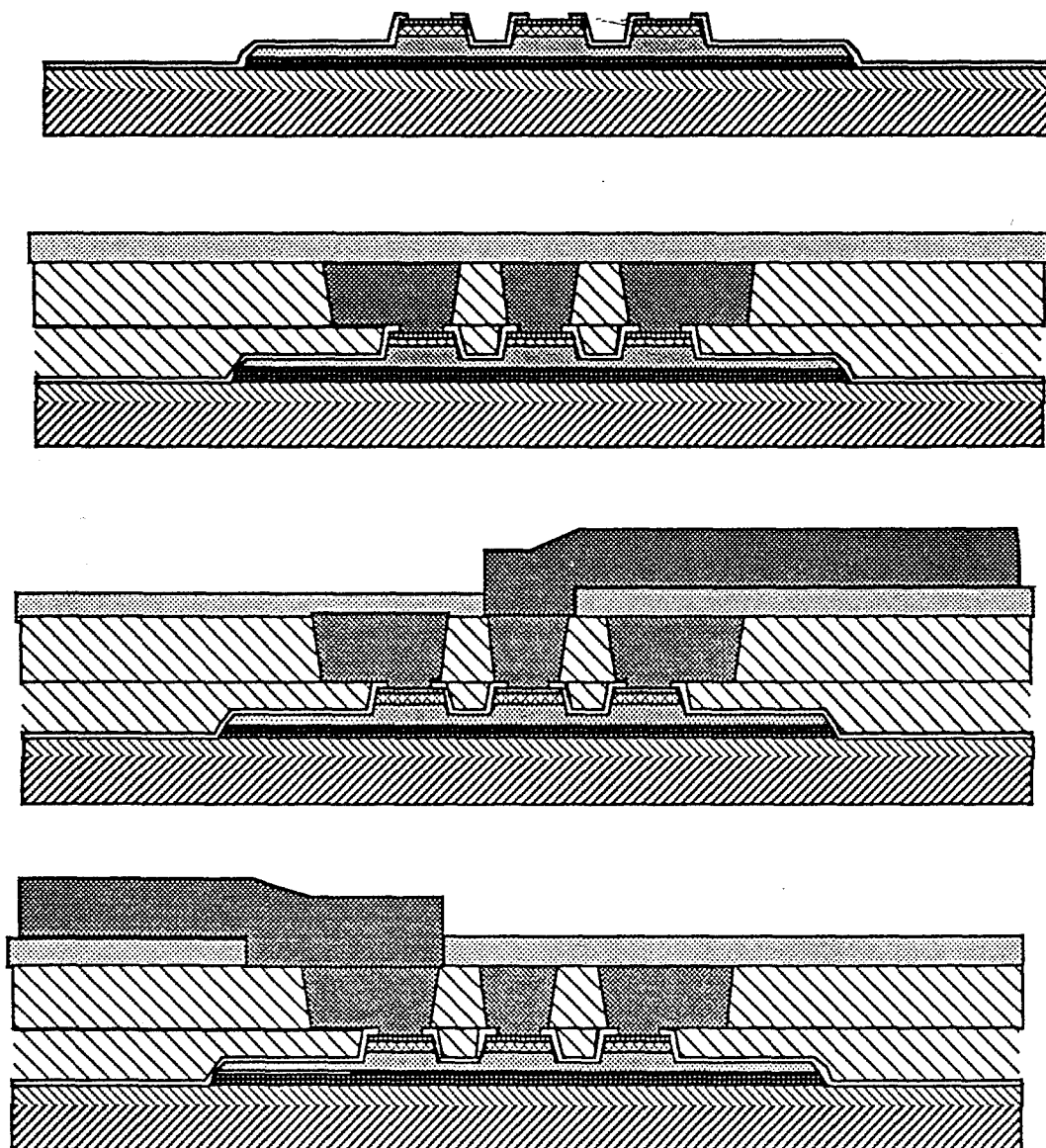


Figure 11 b. Cross-sections at points A to D identified in Fig. 10.

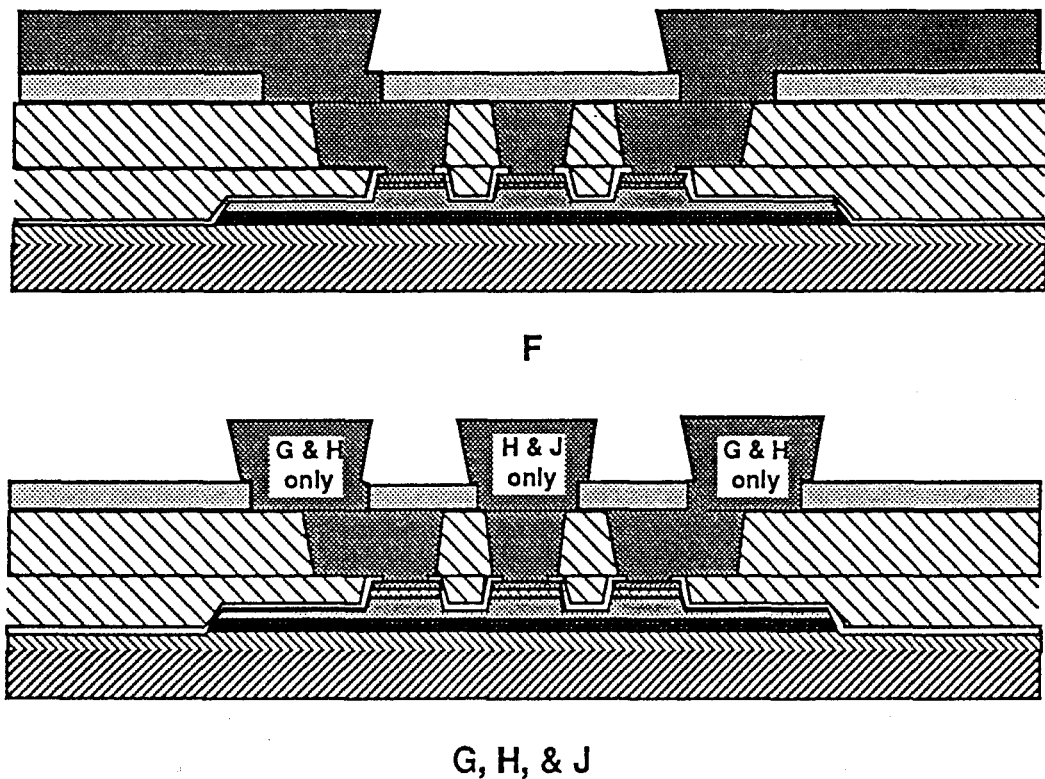


Figure 11 c. Cross-sections at points F to J identified in Fig. 10.

2. Air-Isolated Interconnect Process

In the course of our preliminary fabrication experiments, we discovered that the polyimide did not planarize over the laser structures. Therefore, polyimide will not be used to support the bridge-overs in the three-ridge-guide laser arrays. Air-isolated bridges will be attempted instead. In order to reduce further the capacitance of the bond pad, the p-n junction epilayers outside of the ridge guide area will be etched down an additional micrometer into the substrate. A polyimide mesa, the same height as the ridges, will then be added to support the bonding pads.

The features of this process are: (a) polyimide-isolated bond pads and (b) air-isolated metal bridge interconnects (no polyimide between ridges). Removal of polyimide from between the ridges, in principle, simplifies the process sequence. This process sequence is shown in Fig. 12.

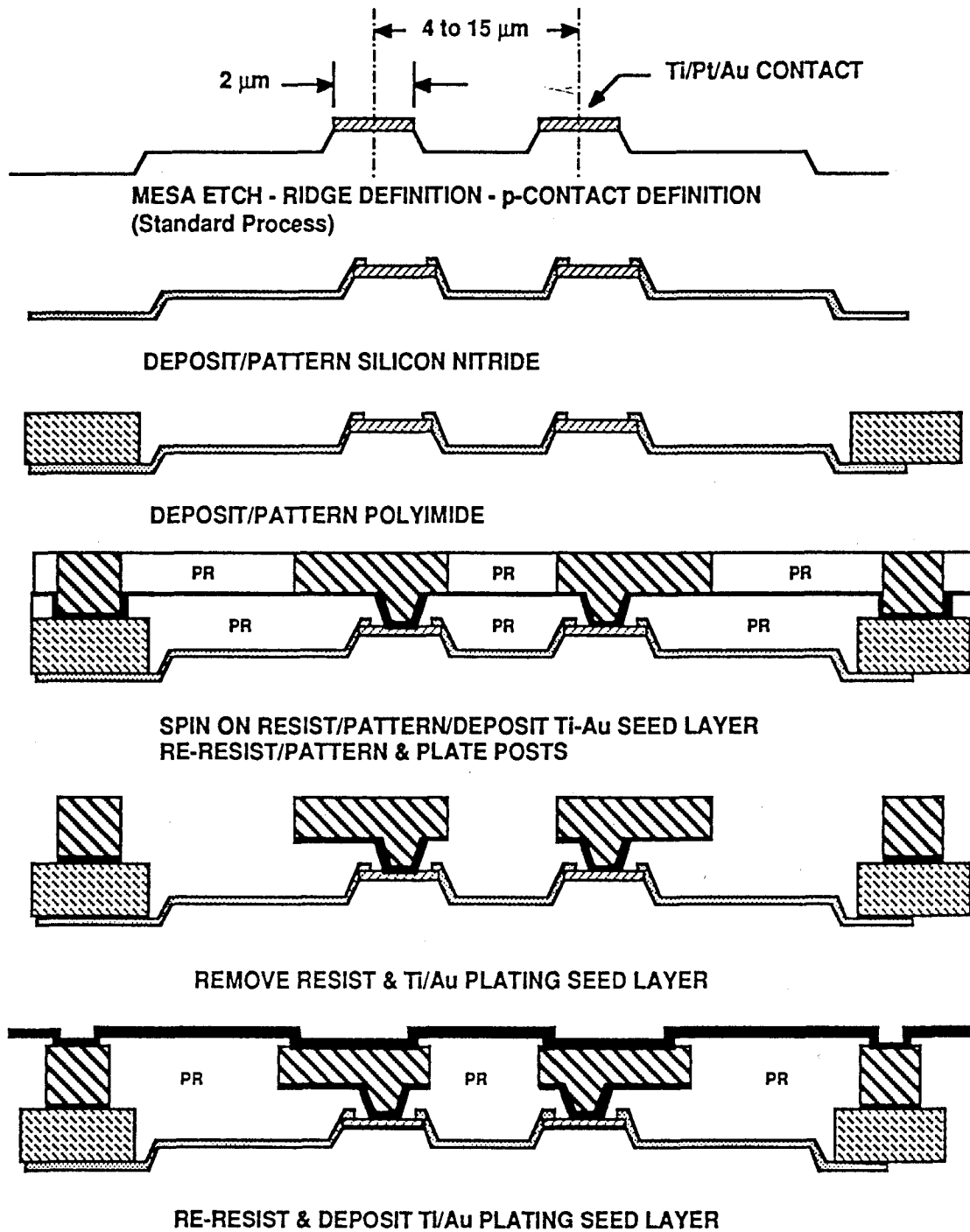


Figure 12. Air-isolated interconnect process.

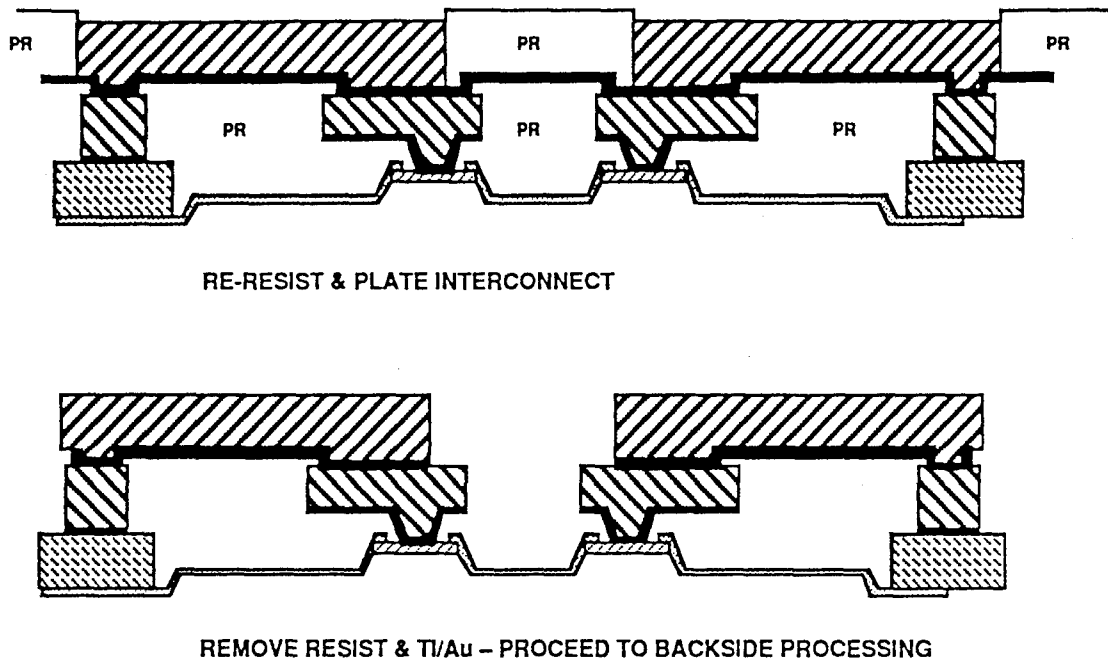


Figure 12. Air-isolated interconnect process (continued).

We were unable to make this process work within the program budget and time constraints. There were topology problems after the first post plating and the interconnect could not be defined. We believe that this is a viable process and with further development effort can be made to work. However, in an attempt to get some results in the program time frame, a simpler process was tried. This process eliminated the use of polyimide and only used Si_3N_4 as the dielectric. While this will result in increased parasitic capacitance, it was felt that for a proof-of-concept validation it would be sufficient to demonstrate experimentally that driving a two-element array 180° out-of-phase will show a response beyond the relaxation oscillation frequency. The objective was to demonstrate experimentally the modulation characteristic shown in Fig. 2.

3. Silicon Nitride Based Process

We re-evaluated our processing strategy for the interconnect, and developed a new process architecture using silicon nitride instead of the polyimide layer. We were successful in defining a $1\text{-}\mu\text{m}$ -thick silicon nitride layer and exposing the p-contact metals on the laser ridge. This process (Fig. 13) appears to be acceptable. Other changes have been introduced. The ridge contact metal thickness was increased. Over the evaporated 400-nm -thick contact metals, an additional $1\text{ }\mu\text{m}$ of Au was plated on top of the ridge structure.

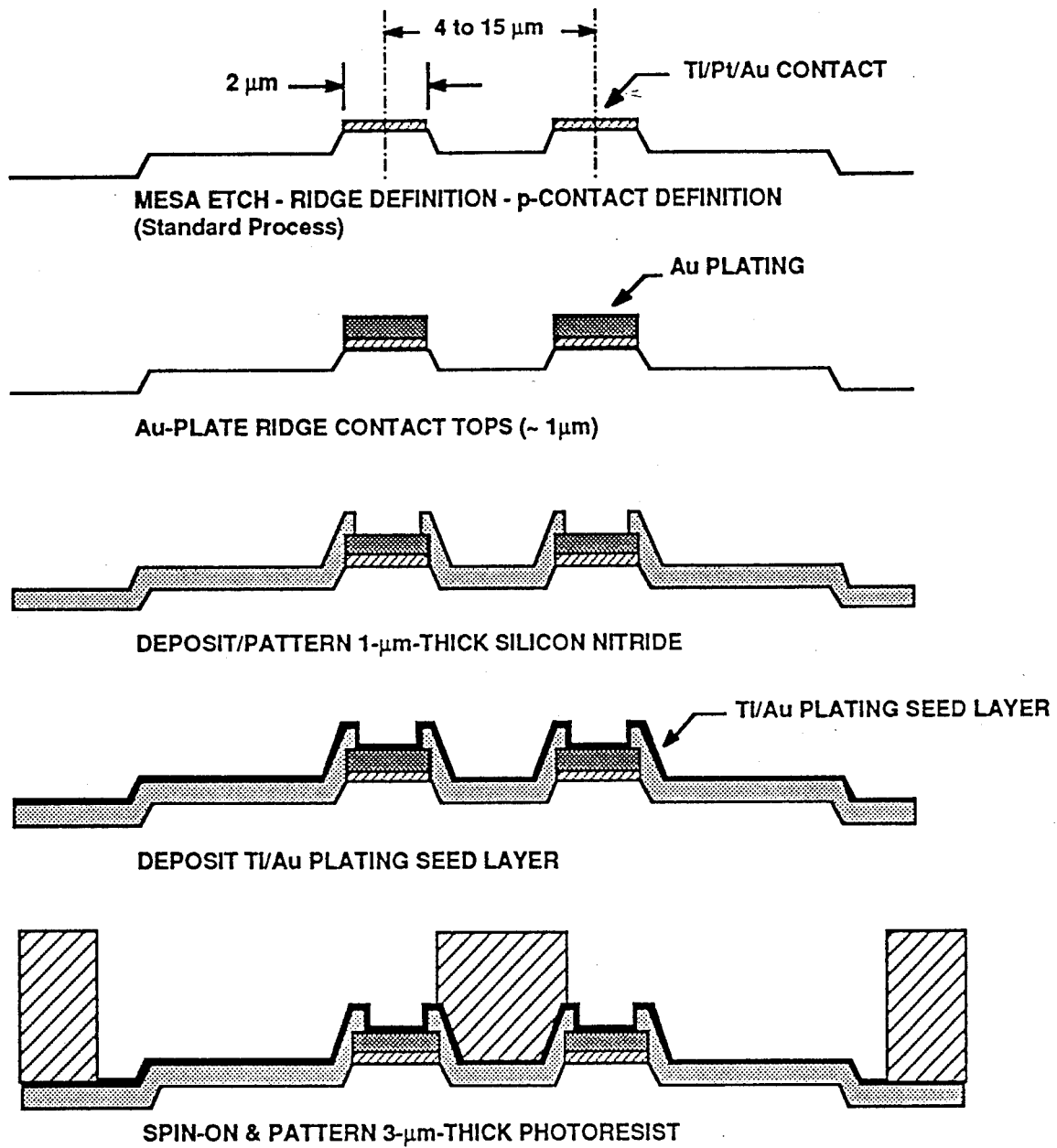


Figure 13. Si_3N_4 isolated process.

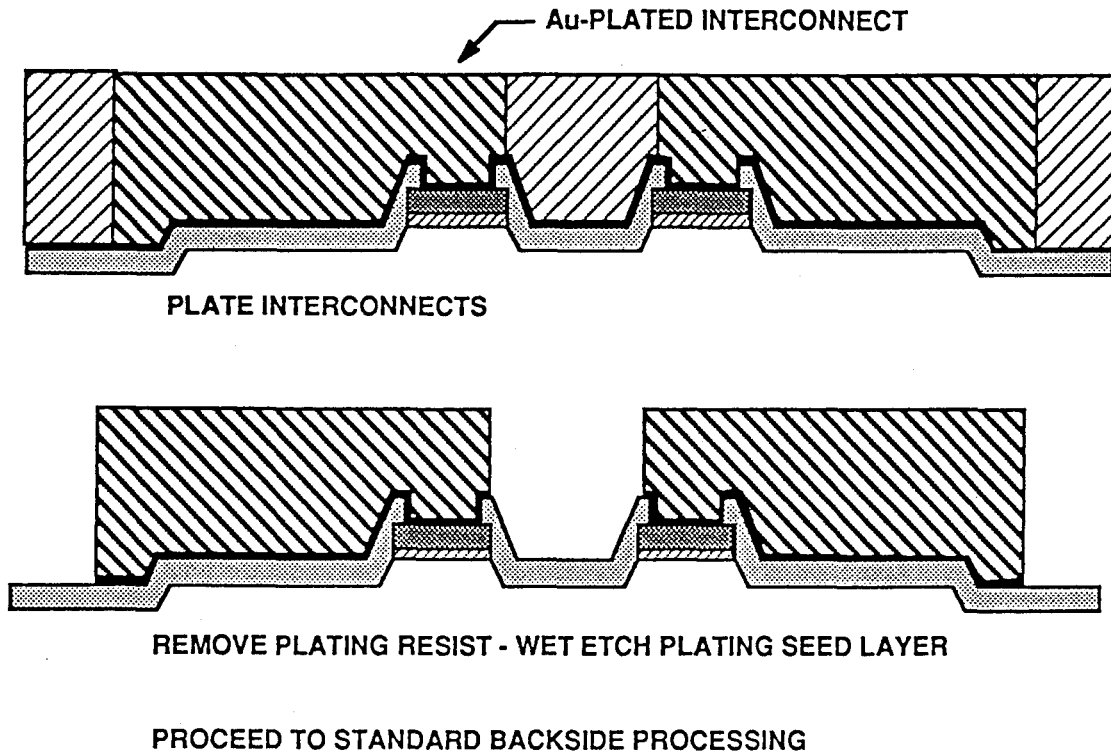


Figure 13. Si_3N_4 isolated process. (continued)

The deposition of the 1- μm nitride layer, resist patterning, and etching of the nitride was successfully completed. A simplified contact plating mask was used and the resist definition and Au plating was completed successfully. It was necessary to use a back-to-front, through-the-wafer alignment (with an IR aligner) to correctly define the required p-contact openings. This required polishing of the n-side of the wafer.

This new p-side processing scheme was successfully completed on a wafer section that was salvaged to determine the viability of this approach without wasting any good material. The salvaged section has very poor morphology and the yield, as expected was low. The processed section was sent to OGI for evaluation.

Two additional wafer sections (good material) are being processed. One wafer was completed and sent to OGI for testing (2/1/94).

E. LASER ARRAY EVALUATION

The plan for evaluating the laser array is described. We intended to carry out an evaluation using a streak camera at OGI and do testing on an automated network analyzer at Sarnoff. Some measurements on the first Si_3N_4 -isolated arrays was done at OGI. Test circuits were designed and fabricated at Sarnoff and a test bench was set up.

We are continuing array fabrication to demonstrate proof-of-concept.

1. Evaluation At Oregon Graduate Institute

The re-worked wafer with the Si_3N_4 -isolated arrays was sent to OGI for testing. The tests carried out are described.

Optical Inspection

Upon receiving the wafer from Sarnoff, a detailed optical inspection was performed. There were 6 rows of lasers. Each row contains a 15-, 10-, 8-, 6-, 5-, and two 4- μm center-to-center spaced arrays. The bottom edge of the wafer (sawed edge) contained unusable devices (labeled row 5). All the devices on the top row, (labeled row 0) had waveguide and metalization alignment problems.

As judged from the optical inspection, ten of the best arrays were mounted and tested. Devices are specified by the row number and element separation value, i.e. '4-15' is the array with a 15- μm element separation in row 4. The tested arrays were:

- Row 4: 6, 8, 10, and 15
- Row 3: 6, 8, 10, and 15
- Row 4: 4, and 5

Current/Voltage Measurement

All devices showed typical diode I/V characteristics, although the turn-on voltage appears high. This is attributed to a high differential series resistance. The first devices tested, 4-15, 4-10, were damaged during I/V measurement on the curve tracer. Pulsed testing was then used. Using pulsed current measurements, the differential series resistance of each element above threshold is $50 \pm 10 \Omega$.

Light/Current Measurement

Four of the ten mounted arrays showed lasing action, and in two of those, a single element dominated. L/I measurements were done for each element separately (where possible) and then with both elements shorted. Initially a 100-ns-wide pulse at 1-kHz PRF was used, but later we changed to a 50-ns pulse at 10-kHz PRF.

- Array 4-6: (elements shorted) Lased with a threshold of 68 mA total current (~34 mA per element), and reached 2 mW peak optical power at 100 mA (50 mA per element).
- Array 3-8: One element lased separately with a 15 mA threshold while the other element did not with currents up to 40 mA. When shorted, the array displayed a threshold of 14 mA per element and the differential efficiency increased slightly when compared to the single element.
- Array 3-10: Element (b) lased with a 6-mA threshold when pumped separately, while element (a) lased at 50 mA. Pumped together, the threshold is 3.5 mA per element and reached 2 mW peak power at 30 mA per element.
- Array 4-4: (contacts shorted) Lased with an array threshold of 90 mA (45 mA per element), and reached 45 mW at 120 mA total current.

The low thresholds for some elements indicates that the wafer material is of high quality. The wide variation of performance, for example, an order of magnitude threshold current difference for elements 10- μm apart, is not known. Perhaps there are nonuniformities or contact problems with the narrow (~3 μm) gold stripe that runs the full length the elements and so only a longitudinal fraction of the laser is actually receiving pump current. The waveguides appear clean and well defined in the samples used for SEM micrographs.

Near-Field Measurement

For arrays 3-8 and 3-10, it was confirmed that the single element which lased with the lower threshold always had a much higher intensity than the other element. These devices are essentially single element lasers for both isolated and shorted pumping.

Array 4-6 displayed a more balanced near-field with comparable intensities from the two elements. However, one element had a significant intensity null resulting in a double-lobed intensity profile, while the other element displayed a smooth Gaussian-like shape. As testing progressed, (during spectral measurements), a null developed in the 'good' element, eventually leading to a near-field containing a pair of double-lobed intensity profiles. The cause for this is not understood, and each of the four lobes is approximately 1.6- μm FWHM.

Spectral Measurement

The one device, Array 4-6, that showed reasonable balanced lasing from both elements was examined using a spectrometer. The center wavelength was 0.955 μm . There are 5 to 10 longitudinal modes running at all times.

Observations at 2nd and 3rd order did not show conclusive evidence of the presence of lateral array modes. The longitudinal modes are slightly asymmetrical, which could be either due

to a weak second lateral mode with <10 GHz splitting or small bit of chirp during the pulse. Resolving power in 3rd order was approximately 5 GHz.

Time Averaged Temporal Measurements

These measurements were carried out using a 20-GHz detector and the CSA803 Communications Analyzer. Array 4-6 displayed very low relaxation oscillations, ranging from 600 to 800 MHz for $1.3 - 1.75 \times I_{th}$ pump current. The relaxation oscillations were fairly undamped taking 7 or 8 oscillations to relax. Later in the pulse (20 to 30 ns) there were erratic oscillations with little correlation between pulses. The primary frequency components in these oscillations is the relaxation oscillation (800 MHz). Single shot observations using the streak camera could not be made (not enough signal for the transient digitizer).

2. Network Analyzer Based Test Setup

The design of a special test fixture for high-speed testing of two-element, lateral-mode-locked lasers was carried out and the test fixture fabricated at Sarnoff. Circuit patterns are shown in Fig. 14. Two RF signals (of equal amplitude but 180° relative phase) drive their respective laser sections through 50-Ω resistors (for broad-band matching to the line impedance). Bias is introduced through a damping resistor in series with a lumped-element choke and is bypassed to ground by a chip capacitor. A large circuit, which measures 6.10×2.03 mm (0.240×0.800 inches) on 0.25-mm-thick alumina, is mounted in a fixture with SMA connectors aligned to the 6- to 18-GHz 180° hybrid. A smaller second circuit, also on 0.25-mm-thick alumina, is mounted with the laser on a sub-mount bolted to the main fixture.

The laser performance will be assessed on an RF/optical test bench. A network analyzer test signal is amplified and split into two equal amplitude, oppositely phased signals.

The signals drive the laser sections and the light from one of the laser sections is focused through a pinhole onto a DC - 60 GHz PIN photodetector (New Focus, Inc.). The light from the other section is blocked. The detected signal is re-amplified and the network analyzer compares it to the initial signal. The network analyzer is calibrated to generate the laser/detector frequency response, removing the amplifier and hybrid responses analytically. The photodetector response, as measured by New Focus, Inc., varies by 2 dB over the 2 to 18 GHz range. This variation with frequency will also be factored out in data analysis.

The 2 to 18 GHz and the 6- to 18-GHz hybrid phase shifters were measured on a network analyzer. In both phase shifters the two arms are within ± 0.7 dB and are within $\pm 5^\circ$ of each other.

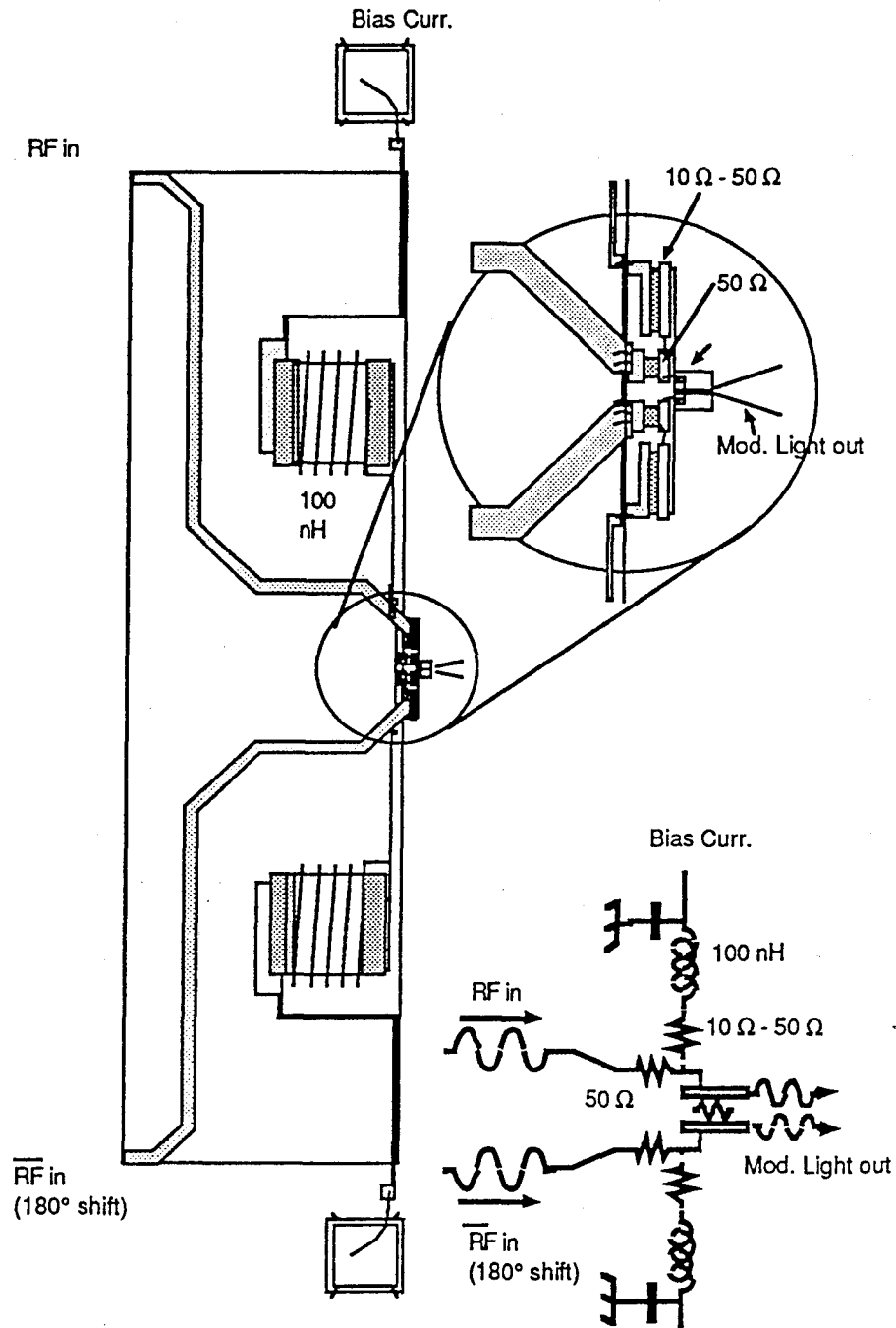


Figure 14. Schematic of test apparatus for lateral mode locked high speed laser.

Preliminary Test Procedure

The following preliminary test procedure was developed for network analyzer testing. The schematic is shown in Fig. 15.

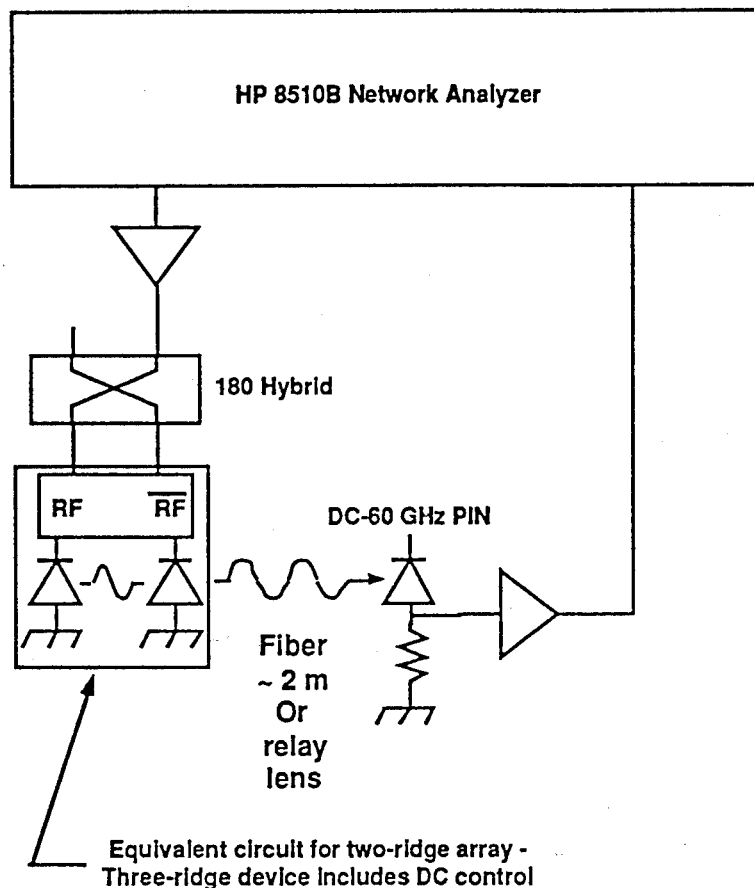


Figure 15. Test schematic for network analyzer measurement.

1. Set up the RF and optics on a small optical bench as shown in Fig. 15. Use a relay lens with 5 to 10 cm focal length (F.L.) and a 2- to 4-cm diameter clear aperture on an X-Y mount (or a fixed mount). Use a 5- μm -diameter pinhole on the XYZ mount and a single-mode fiber on a separate XYZ mount.
2. Select and mount bars or chips in test fixture. Make sure that there is no chance of any reflections into the back facet. Include a set of RF calibration standards.
3. Mount the test fixture onto a block (no RF connection yet) and roughly align the lens and the pinhole. Turn on each laser stripe separately and complete alignment to the pinhole. Align for maximum power (PIN DC current) and maximum isolation between laser images.

Do a P/I curve (optical power as function of diode current). Measure the DC parameters and determine initial DC bias point and RF power levels.

4. Calibrate the HP 8510 Network Analyzer through the RF portions of the equipment. Use ~ 30 dB attenuator to simulate the laser/PIN.
5. Apply DC bias and RF drive to laser sections under several conditions:
 - (a) Control I: Single laser section under DC and RF. The normal relaxation oscillation peak should be seen. Measure the characteristics as a function of laser bias current.
 - (b) Control II: Single laser section under DC and RF, with the other section under DC only. Both relaxation oscillation peak and the lateral mode beat resonance should be seen. Vary the DC and RF to separate the two effects.
 - (c) Control III: Both laser sections with equal DC and equal, in-phase (Sigma), RF through the hybrids. The relaxation oscillation response should be observed as in Control I, with slightly reduced response due to additional heating. The response should have 1 to 2 dB more ripple below the relaxation frequency than in Control I, since the hybrids and the laser sections will have unequal frequency responses. The ripple should be more pronounced above the relaxation frequency.
 - (d) Proof-of-Concept Experiment: Both laser sections equal DC and equal, 180°-phase (Delta), RF through hybrids. The high frequency beat response peaking well above the relaxation oscillation frequency should be seen.

F. CONCLUSIONS

Rate equation theory predicts that inter-element-coupling in semiconductor laser arrays introduces new time constants into the laser's dynamical system. This phenomenon is related to the beating between *lateral* array modes and takes place at frequencies from 10 to 50 GHz for typical array designs employing index-guided laser elements.

Linearized analysis of coupled laser rate equations has shown that the array system can be asymptotically stable for values of the coupling attainable with practical index-guided lasers. The small-signal responsivity for a two-element array, for 180° out-of-phase (anti-symmetric) modulation, extends far beyond the relaxation oscillation frequency *when examining the optical output from a single element*.

We use the full rate equation theory for large signal analysis and theoretically demonstrate potential schemes for utilizing these microwave frequency resonances for high-speed optical signal transmission. We show that digital signals with bit rates many times the relaxation oscillation frequency can be transmitted. The width of the inter-element responsivity resonance can also be exploited for encoding analog information using narrow band amplitude modulation (sub-carrier multiplexing - SCM).

To utilize the inter-element time constants for communications applications while suppressing relaxation oscillations, the coupled system must be maintained at dynamical equilibrium. The high-speed transfer of energy between array elements is stimulated by fast anti-symmetric drive level changes, but the original equilibrium must then be quickly restored otherwise the system begins to relax towards a new equilibrium and experiences relaxation oscillations. The type of binary signal used must be appropriately chosen to ensure that the equilibrium is regularly enforced for arbitrary bit patterns. With an anti-symmetric Non-Return-to-Zero (NRZ) encoding scheme, a series of binary '1's could result in periods of asymmetric drive levels sufficiently long for the system to relax towards a new asymmetric equilibrium. Digital signals should therefore be implemented in a return-to-zero (RZ) or similar scheme where the drive signal regularly returns to the original bias condition.

We considered the case of a 0101101110 RZ digital pattern, and our computations show that it can be implemented at *a bit rate of 25 Gb/s*. This digital signal was conditioned by the addition of an overshoot on the return transition to ensure a fast return to the initial dynamic equilibrium. *The relaxation oscillation frequency for the lasers in this two-element array is nominally 4 GHz*.

The width of the inter-element responsivity resonance can also be exploited for encoding analog information using narrow-band amplitude modulation (sub-carrier multiplexing - SCM).

We considered the example of a 44 GHz carrier with a 1-GHz amplitude modulated envelope signal, and our computation shows such a modulation can be successfully implemented (same device parameters as used for the digital example). The digital and analog results described above are examples that were chosen ad hoc and do not represent the performance limits.

Two- and three-element strained InGaAs/AlGaAs single-quantum-well laser arrays were designed. The lasers in these arrays were of a ridge waveguide geometry, a design with which Sarnoff has extensive experience. The key device design and fabrication task in this program was to design and implement a low parasitic electrode structure. The three-element array requires cross-overs for the electrodes and is thus more complicated.

Process architectures for the fabrication of these arrays were generated and process development begun. It was not possible to implement the polyimide-isolated structure with the minimum parasitics within the program time and budget constraints. The major problem encountered was that we were unable to planarize the twin-ridge waveguide structure using polyimide.

Towards the end of this program phase, we carried out a literature search and found that a new class of organic dielectrics, benzocyclobutenes (BCB) are superior to polyimides for planarization and are now used in the fabrication of multi-chip modules [10]. It is recommended that BCB be investigated in the next program phase for planarization.

In summary, our theoretical studies have shown that this concept has merit. There is currently a significant effort on increasing the relaxation oscillation frequency of multi-quantum-well semiconductor lasers by appropriately tailoring the transport properties of the laser layers. These advances can be incorporated in the array element design leading to higher modulation rates. *It must be emphasized that processes for the high-yield fabrication of low-parasitic structures must be developed to realize optical sources with high extrinsic modulation capabilities.* Just demonstrating increased intrinsic capability by calibrating out the effect of parasitic reactances is not enough. It is also necessary to determine the effect of the array on RIN properties, the use of multiple (> 3) element arrays, the dynamic range that can be obtained, and other performance parameters that are important to *system* performance.

G. RECOMMENDATIONS

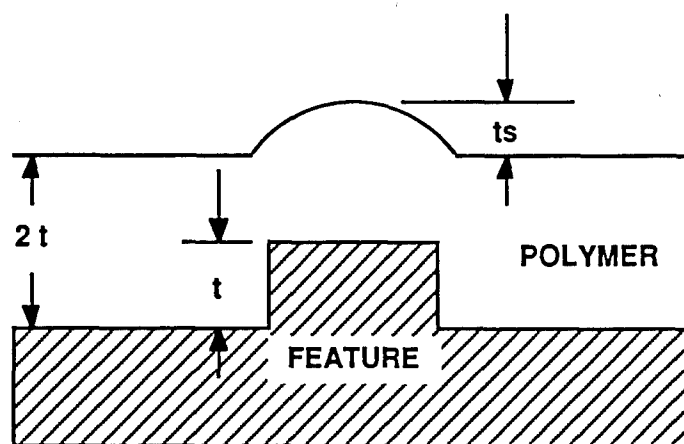
Further study is recommended to optimize the array and understand and quantify the performance capabilities and limitations. Performance parameters that are of interest for microwave systems such as noise figure, linearity, and spur-free dynamic range must be studied both theoretically and experimentally.

The major fabrication problem encountered was that we were unable to planarize the laser array structure using polyimide. This prevented us from fabricating a low-parasitic array structure with reasonable yield. Test structures were fabricated for concept validation by using silicon nitride as the intermetal dielectric.

Towards the end of this program phase, we carried out a literature search and found that a new class of organic dielectrics, benzocyclobutenes (BCB) are superior to polyimides for planarization and are now used in the fabrication of multi-chip modules [10]. The attractive properties of these materials are:

- Low dielectric constant of 2.7 - leading to 20% lower capacitance than for a comparable polyimide structure.
- Loss tangent of 0.002 at 10 GHz.
- Lower water absorption than for polyimides.
- High degree of planarization - > 90 % compared to ~ 18 - 30% for polyimides.

Degree of planarization (DOP) is defined as the step height resulting after dielectric deposition and cure vs. the initial step height of the pattern (Fig. 16).



$$DOP = 100 \times (t - ts) / t$$

Figure 16. Degree of planarization (DOP).

- Polymerization is purely thermal and does not produce volatiles, in contrast to polyimides which produce water. This leads to shrinkage during curing of < 5% compared to ~ 25% for polyimides.
- Can be fully cured in nitrogen at 250°C.

It is recommended that BCB be investigated in the next program phase for planarization.

In summary, our theoretical studies have shown that this concept has merit. There is currently a significant effort on increasing the relaxation oscillation frequency of multi-quantum-well semiconductor lasers by appropriately tailoring the transport properties of the laser layers. These advances can be incorporated in the array element design leading to higher modulation rates. *It must be emphasized that processes for the high-yield fabrication of low-parasitic structures must be developed to realize optical sources with high extrinsic modulation capabilities.* Just demonstrating increased intrinsic capability by calibrating out the effect of parasitic reactances is not enough. It is also necessary to determine the effect of the array on RIN properties, the use of multiple (> 3) element arrays, the dynamic range that can be obtained, and other performance parameters that are important to *system* performance.

REFERENCES

1. K. Y. Lau, "Narrow-Band Modulation of Semiconductor Lasers at Millimeter Wave Frequencies (> 100 GHz) by Mode Locking," *IEEE J. Quantum Electron.*, 26(2), 250-261, Feb. 1990.
2. R. Nagarajan, et al., "Resonantly Enhanced Semiconductor Lasers for Efficient Transmission of Millimeter Wave Modulated Light," *IEEE Photon. Technol. Lett.*, 5(1), 4-6, Jan. 1993.
3. R. K. DeFreez, N. Yu, D. J. Bossert, M. Felisky, G. A. Wilson, R. A. Elliott, H. G. Winful, G. A. Evans, N. W. Carlson, and R. Amantea, "Experimental Characterization of the Picosecond Spatio-temporal Properties of Coherent Semiconductor Laser Arrays," *Proc. Opt. Soc. Amer. - Topical Meeting on Nonlinear Dynamics in Optical Systems*, Afton, OK, 1990, Paper ThAI.
4. S. S. Wang and H. G. Winful, "Dynamics of Phase-Locked Semiconductor Laser Arrays", *Appl. Phys. Lett.*, 52, 1776-1774, 23 May 1988.
5. H. G. Winful and S. S. Wang, "Stability of Phase Locking in Coupled Semiconductor Laser Arrays", *Appl. Phys. Lett.*, 53(20), 1894-1896, 14 Nov. 1988.
6. G. A. Wilson, R. K. DeFreez, and H. G. Winful, "Modulation of Twin-Emitter Semiconductor Lasers Beyond The Frequency of Relaxation Oscillations," *Opt. Comm.*, 82(3-4), 293-298, April 1991.
7. G. A. Wilson, R. K. DeFreez, and H. G. Winful, "Modulation of Phased-Array Semiconductor Lasers at K-Band Frequencies," *IEEE J. Quantum Electron.*, 27, 1696-1704, June 1991.
8. G. P. Agrawal, "Effect of Gain and Index Nonlinearities on Single-Mode Dynamics in Semiconductor Lasers", *IEEE J. Quantum Electron.*, 26(11), 1901-1909, Nov. 1990.
9. E. Kapon, J. Katz, and A. Yariv, "Supermode Analysis of Phase-Locked Arrays of Semiconductor Lasers," *Opt. Lett.*, 10, 1984, pp. 125-127.
10. D. Burdeaux, et al., "Benzocyclobutene (BCB) Dielectrics for the Fabrication of High Density, Thin Film Multichip Modules," *J. Electron. Mater.*, 19(12), 1357-1366, December 1990.

DISTRIBUTION LIST

addresses	number of copies
ROME LABORATORY/OCPC ATTN: ERNST K. WALGE 25 ELECTRONIC PKY GRIFFISS AFB NY 13441-4515	2
DAVID SARNOFF RESEARCH CENTER, INC. 201 WASHINGTON RD PRINCETON, NJ 08543	4
RL/SUL TECHNICAL LIBRARY 26 ELECTRONIC PKY GRIFFISS AFB NY 13441-4514	1
ADMINISTRATOR DEFENSE TECHNICAL INFO CENTER DTIC-FDAC CAMERON STATION BUILDING 5 ALEXANDRIA VA 22304-6145	2
ADVANCED RESEARCH PROJECTS AGENCY 3701 NORTH FAIRFAX DRIVE ARLINGTON VA 22203-1714	1
NAVAL WARFARE ASSESSMENT CENTER GIDEP OPERATIONS CENTER/CODE QA-50 ATTN: E RICHARDS CORONA CA 91718-5000	1
ASC/ENEMS WRIGHT-PATTERSON AFB OH 45433-6503	1
AFIT/LDEE 2950 P STREET WRIGHT-PATTERSON AFB OH 45433-6577	1

WRIGHT LABORATORY/MLPO 1
ATTN: D.L. DENISON
WRIGHT-PATTERSON AFB OH 45433-6533

WRIGHT LABORATORY/MTEL 1
WRIGHT-PATTERSON AFB OH 45433

AUL/LSE 1
BLDG 1405
MAXWELL AFB AL 36112-5564

COMMANDING OFFICER 1
NAVAL AVIONICS CENTER
LIBRARY D/765
INDIANAPOLIS IN 46219-2189

COMMANDING OFFICER 1
NCCOSC ROTE DIVISION
CODE 0274B, TECH LIBRARY
53560 HULL STREET
SAN DIEGO CA 92152-5001

CMOR 1
NAVAL WEAPONS CENTER
TECHNICAL LIBRARY/C3431
CHINA LAKE CA 93555-6001

CDR, U.S. ARMY MISSILE COMMAND 2
REDSTONE SCIENTIFIC INFO CENTER
AMSMI-RD-CS-R/ILL DOCUMENTS
REDSTONE ARSENAL AL 35898-5241

ADVISORY GROUP ON ELECTRON DEVICES 2
ATTN: DOCUMENTS
2011 CRYSTAL DRIVE, SUITE 307
ARLINGTON VA 22202

REPORT COLLECTION, RESEARCH LIBRARY 1
MS P364
LOS ALAMOS NATIONAL LABORATORY
LOS ALAMOS NM 87545

COMMANDER/USAISC 1
ATTN: ASOP-DO-TL
BLDG 61801
FT HUACHUCA AZ 85613-5000

SOFTWARE ENGINEERING INST (SEI) 1
TECHNICAL LIBRARY
5000 FORBES AVE
PITTSBURGH PA 15213

NSA 1
ATTN: D. ALLEY
DIV X911
9800 SAVAGE ROAD
FT MEADE MD 20755-6000

DDO 1
R31
9800 SAVAGE ROAD
FT. MEADE MD 20755-6000

DIRNSA 1
R509
9800 SAVAGE ROAD
FT MEADE MD 20775

DEFENSE TECHNOLOGY SEC ADMIN (DTSA) 1
ATTN: STTD/PATRICK SULLIVAN
400 ARMY NAVY DRIVE
SUITE 300
ARLINGTON VA 22202

ATTN: DAVID D. CURTIS 1
ROME LABORATORY/ERAA
HANSCOM AFB, MA 01731-5000

ATTN: J. BRUCE THAXTER 1
ROME LABORATORY/ERAC
HANSCOM AFB, MA 01731-5000

ATTN: RICHARD PAYNE 1
ROME LABORATORY/ERO
HANSCOM AFB, MA 01731-5000

ATTN: JOSEPH P. LORENZO, JR. 1
ROME LABORATORY/ERDC
HANSCOM AFB, MA 01731-5000

ATTN: JOSEPH L. HORNER 1
ROME LABORATORY/EROP
HANSCOM AFB, MA 01731-5000

ATTN: RICHARD A. SOREF 1
ROME LABORATORY/EROC
HANSCOM AFB, MA 01731-5000

ATTN: JOHN J. LARKIN 1
ROME LABORATORY/ERXE
HANSCOM AFB, MA 01731-5000

ATTN: DANIEL J. BURNS 1
ROME LABORATORY/ERDD
525 BROOKS RD
GRIFFISS AFB NY 13441-4505

ATTN: ALBERT A. JAMBERDINO 1
ROME LABORATORY/IRAP
32 HANGAR RD
GRIFFISS AFB NY 13441-4114

ATTN: BRIAN M. HENDRICKSON 1
ROME LABORATORY/OCP
25 ELECTRONIC PKY
GRIFFISS AFB NY 13441-4515

ATTN: GREGORY J. ZAGAR 1
ROME LABORATORY/OCPC
25 ELECTRONIC PKY
GRIFFISS AFB NY 13441-4515

ATTN: ROBERT L. KAMINSKI 1
ROME LABORATORY/C38C
525 BROOKS RD
GRIFFISS AFB NY 13441-4505

ATTN: DONALD W. HANSON 1
ROME LABORATORY/OC
26 ELECTRONIC PKY
GRIFFISS AFB NY 13441-4514

ATTN: JAMES W. CUSACK 1
ROME LABORATORY/DCP
25 ELECTRONIC PKY
GRIFFISS AFB NY 13441-4515

ATTN: JOANNE L. ROSSI 1
ROME LABORATORY/DCP
25 ELECTRONIC PKY
GRIFFISS AFB NY 13441-4515

ATTN: ANDREW R. PIRICH 1
ROME LABORATORY/DCPA
25 ELECTRONIC PKY
GRIFFISS AFB NY 13441-4515

ATTN: RICHARD J. MICHALAK 1
ROME LABORATORY/OCPB
25 ELECTRONIC PKY
GRIFFISS AFB NY 13441-4515

DC TECHNICAL LIBRARY 1
ROME LABORATORY/OC
26 ELECTRONIC PKY
GRIFFISS AFB NY 13441-4514

NY PHOTONIC DEVELOPMENT CORP 1
MVCC ROME CAMPUS
UPPER FLOYD AVE
ROME, NY 13440

ROME LABORATORY/OC 1
26 ELECTRONIC PKY
GRIFFISS AFB NY 13441-4514

MISSION
OF
ROME LABORATORY

Mission. The mission of Rome Laboratory is to advance the science and technologies of command, control, communications and intelligence and to transition them into systems to meet customer needs. To achieve this, Rome Lab:

- a. Conducts vigorous research, development and test programs in all applicable technologies;
- b. Transitions technology to current and future systems to improve operational capability, readiness, and supportability;
- c. Provides a full range of technical support to Air Force Materiel Command product centers and other Air Force organizations;
- d. Promotes transfer of technology to the private sector;
- e. Maintains leading edge technological expertise in the areas of surveillance, communications, command and control, intelligence, reliability science, electro-magnetic technology, photonics, signal processing, and computational science.

The thrust areas of technical competence include: Surveillance, Communications, Command and Control, Intelligence, Signal Processing, Computer Science and Technology, Electromagnetic Technology, Photonics and Reliability Sciences.